

SIMULATING CHERENKOV RADIATION
GENERATED BY RADIOTHERAPY BEAMS

A Dissertation
presented to
the Faculty of the Graduate School
at the University of Missouri-Columbia

In Partial Fulfillment
of the Requirements for the Degree
Doctor of Philosophy

by
ANDY N. WILES
Dr. Enrique W. Izaguirre and Dr. Sudarshan K. Loyalka,
Dissertation Supervisors

December 2017

APPROVAL PAGE

The undersigned, appointed by the dean of the Graduate School, have examined the dissertation entitled

SIMULATING CHERENKOV RADIATION
GENERATED BY RADIOTHERAPY BEAMS

presented by Andy Wiles,

a candidate for the degree of doctor of philosophy,

and hereby certify that, in their opinion, it is worthy of acceptance.

Dr. Enrique Izaguirre

Dr. Sudarshan Loyalka

Dr. Lixin Ma

Dr. Tushar Ghosh

Dr. Mark Prelas

Dr. Robert Tompson

For my supportive parents,
my loving and patient wife,
and my joyful daughter.

ACKNOWLEDGEMENTS

I would like to acknowledge the support for this work provided through the Graduate Assistance in Areas of National Need (GAANN) fellowship from the U.S. Department of Education.

I would like to thank my advisors, Dr. Enrique Izaguirre and Dr. Sudarshan Loyalka, for their thoughtful feedback and knowledgeable guidance on pursuing this research. Their combined expertise provided a stable foundation on which to build my own knowledge.

I would like to thank all of my committee members, Dr's Tushar Ghosh, Mark Prelas, Robert Tompson, and Lixin Ma, and all of the current and former faculty members of NSEI for providing outstanding education throughout my graduate studies at the University of Missouri.

I would also like to express my appreciation to the NSEI staff, Latricia Vaughn and James Bennett, who helped me navigate my graduate school experience from start to finish, and I am grateful for their prompt responses to every issue that arose during the course of my graduate studies.

TABLE OF CONTENTS

ACKNOWLEDGEMENTS.....	ii
LIST OF TABLES	vi
LIST OF FIGURES.....	viii
ABSTRACT	xvi
CHAPTER 1: General Introduction	1
I. Introduction.....	1
II. Background.....	5
III. Thesis Organization	9
IV. References	10
CHAPTER 2: Literature Review	12
I. Scintillation fibers.....	12
II. Cherenkov imaging in tissue.....	16
III. References.....	21
CHAPTER 3: Contribution of Cherenkov radiation in scintillator fiber detectors	25
I. Introduction.....	26
II. Methods.....	30
III. Technical characteristics of simulated fibers and detectors	42
IV. Results.....	48
V. Discussion.....	56
VI. Conclusions	60

VII. References.....	60
CHAPTER 4: A two-layer cutaneous tissue model of external beam radiotherapy induced Cherenkov emission	64
I. Introduction.....	65
II. Methods.....	66
III. Results	75
IV. Discussion	90
V. Conclusions.....	96
VI. Acknowledgments.....	98
VII. References.....	98
CHAPTER 5: External electron beam induced Cherenkov emission from the two-layer cutaneous tissue model.....	101
I. Cherenkov emission for electron beams and sensitivity to tissue parameters	101
II. Sensitivity of Cherenkov emission to surface lesion tissue parameters for electron beams.....	108
III. Conclusions.....	110
CHAPTER 6: General Conclusions	112
I. General Discussion.....	112
II. Recommendations for future research.....	115
VITA	116

LIST OF TABLES

Table 3-I. Simulation model parameters.	49
Table 3-II. Photon detection numbers show the signal per MeV and Cherenkov photon contribution to the total signal for each of the pairings of BCF-60 and BCF-12 with the two photodetectors...	52
Table 3-III. Cherenkov distribution relative to the scintillation emission spectra for the two detector technologies paired with each of the two fiber formulations. The percentage of Cherenkov light with shorter wavelengths than the shortest scintillation wavelength and with longer wavelengths than the longest scintillation wavelength depends on the detector sensitive range and the scintillation distribution range.	54
Table 4-I. Signal-to-noise ratio of Cherenkov radiation emission in de-oxygenated skin lesions. Variation with melanin is parameterized into light, medium, and dark skin. Two principle wavebands, 586-796nm and 454-500nm, are compared for each skin type.....	95
Table 5-I. Signal-to-noise ratio of Cherenkov radiation emission in de-oxygenated skin lesions for an incident electron beam containing 10^4 electrons. Variations with melanin are parameterized into light, medium, and dark skin for different epidermal	

melanosome volume percentages and for the 586-796nm and
454-500nm wavebands. 110

LIST OF FIGURES

Figure 3-1: Diagram of the detector containing a round scintillation fiber embedded between two plates of acrylic..... 32

Figure 3-2. The rate of electron interactions in polystyrene fiber core material per unit pathlength as a function of the electron's kinetic energy in MeV. Scintillation is shown for an average scintillation yield of 7100 photons per MeV of deposited energy. Cherenkov photons are restricted to the wavelength range of 300 nm to 1200 nm, which is the upper spectral response of a silicon photodiode and does not account for 25% of the total Cherenkov light that would be produced above 1200 which is out of the detector range. Electron scatter accounts only for elastic scattering by soft Coulomb collisions..... 35

Figure 3-3. Cherenkov radiation spectrum over the wavelength range of interest in the model, 300 nm to 1200 nm. The spectrum is shown for electron velocities from 0.7c, just above the threshold for Cherenkov radiation production, in 0.1c increments up through 1.0c, the theoretical maximum electron velocity, although for clinical 6MV beams, the maximum is 0.997c and the minimum energy to produce Cherenkov radiation occurs at 0.15 MeV. The shaded region of the figure overlaps the scintillation light produced with clinical beams. 37

Figure 3-4. The emission angles of Cherenkov photons are distributed in a cone with its axis along the propagation vector Ω_e . Ω_p is the photon vector and θ_p is the cone emission angle 39

Figure 3-5: The reflection angles of Cherenkov photons at the fiber boundary are determined by the surface normal (surface perpendicular to x-axis shown here) and remain constant for a given photon. 41

Figure 3-6. Normalized emission spectra for the BCF-12 and BCF-60 scintillator fibers. BCF-12 has a broad spectrum that peaks at 435 nm in the blue region of the visible spectrum and BCF-60 has a narrow emission in the green region of the visible spectrum with a maximum at 530 nm..... 44

Figure 3-7. Transmission distribution used in the simulation based on a semi-empirical model of the bulk material properties of polystyrene. The plot shows the transmitted fraction of an initially uniform wavelength distribution after propagating through 100 cm of polystyrene material..... 46

Figure 3-8. Modeled photodetectors. The photodiode was modeled with cubic spline interpolation of the data points, and it has a wide spectral sensitivity range with a 0.62 A/W peak spectral sensitivity at 850 nm. The SiPM was modeled with linear interpolation, and it has a narrow sensitivity range with a 0.48 peak detection efficiency at 450 nm. The curves are normalized to their peak

value. Signal output for a photodiode is typically 1-10, while the silicon photomultiplier output increases with gain on the order of 10^6	47
Figure 3-9. The percent of Cherenkov photons in the detected light in a square fiber and round fiber at different gantry angles for 6 MeV electrons and 6 MV photons. The detecting photodiode is at 22.5 cm from the isocenter in the direction of the gantry position at 90 degrees, and the fiber passes through the isocenter.	50
Figure 3-10. Experimental measurements of light output from an un-doped optical fiber irradiated by 6MV x-rays and coupled to a PMT follow the predicted curve from simulations.	51
Figure 3-11. The spectrum of Cherenkov photons detected by the photodiode and the SiPM.	53
Figure 3-12. The fraction of Cherenkov photons in the detected light for electrons with incident energy of 1 to 20 MeV.	55
Figure 3-13. The number of photons detected per absorbed MeV decreases with decreased width of the fiber, where the width is diameter for round fibers and edge length for square fibers.	56
Figure 4-1. Diagram of the two-layer skin model with a 0.1 mm thick epidermal layer overlying the dermal layer.	69
Figure 4-2. Wavelength-dependent optical interaction coefficients for human skin in the visible range and extending out to 1000nm.	

Epidermal absorption occurs by melanin, dermal absorption occurs by a mixture of oxygenated hemoglobin (HbO₂), deoxy-hemoglobin (Hb), and water. Reduced scattering coefficients for the epidermis and dermis are also shown. 72

Figure 4-3. Cherenkov intensity distributions at the moment of generation in the media for radiation beamlets impinging at normal incidence into an air-medium interface. For both figures the vertical axis shows depth in tissue, with the air boundary at the top (depth=0), extending downward to a depth of 4mm, and the horizontal axis shows the transverse cross-section through the center of the 1 mm² 6-MV x-ray beamlet. The medium on the left (a) is tissue and on the right (b) is water..... 77

Figure 4-4. Top down views of the air-tissue surface centered at the 1x1 mm² beamlet, with insets showing the horizontal profile line through the center of each corresponding plot. a) Isodose distribution contours showing the average dose in the upper 4 mm tissue layer for the 6 MV photon beam, b) the corresponding Cherenkov emission intensity from the tissue at the surface, and (c) backscattered light for a normal incidence optical beam. Normalization is to maximum intensity and the dimensions are in mm. 79

Figure 4-5. Emitted intensity plot of the directional distribution per unit solid angle (Sr^{-1}) of emitted light with 5 degree binning. The surface normal is designated as 90 degrees. Curves are each normalized to a total photon emission of unity before calculating the emission per solid angle. 80

Figure 4-6. The photon spectral distribution of the emitted light ranging in wavelength from 350nm to 1000nm for Cherenkov emission from the skin, Cherenkov from water, and diffusely reflected optical light from the skin model. The vertical axis is normalized to emitted photons per incident particle (either Cherenkov photons per x-ray or diffusely reflected photons per incident photon). 82

Figure 4-7. Cherenkov radiation spectrum emitted from skin with 10nm binning. Skin parameters are set to 40% oxygen saturation and a range of epidermal melanosome volume fraction from 0.013 to 0.45. 84

Figure 4-8. The Cherenkov intensity in the 454-500nm wavelength band as a function of oxygen saturation. The curves are parameterized to the melanosome volume fraction, ranging from 1.3% to 45%.... 86

Figure 4-9. The Cherenkov intensity in the 586-796nm wavelength band a function of oxygen saturation. The curves are parameterized to the melanosome volume fraction, ranging from 1.3% to 45%.... 87

Figure 4-10. Emitted Cherenkov intensity per incident particle as a function of melanosome volume fraction. Curves are plotted for fully deoxygenated hemoglobin (0% SO₂), fully oxygenated hemoglobin (100% SO₂), and the average over all SO₂ values. The intensity curves are shown separately for Cherenkov radiation generated in the 454-500nm range and the 586-796nm range. 89

Figure 4-11. Cherenkov surface emission distributions in the 586-796nm waveband and the 454-500nm waveband, with 20% SO₂ in the central 3cm diameter circle of each image and 40% SO₂ baseline in the surrounding surface. The images are normalized to equal intensity in the 40% SO₂ surrounding surface, and the normalization factor shows the increasing relative imaging exposure time to compensate for absorption by increased melanin content and the sensitivity of each waveband. Variations are shown for light, medium, and dark skin containing, respectively, 2.5%, 15%, and 30% melanosome volume fraction of the epidermis. The grayscale units are total emitted Cherenkov photons per mm² for an incident 6MV beamlet of fluence 10⁶ x-rays per mm², multiplied by the relative exposure time shown above each image. 92

Figure 4-12. Cherenkov surface emission distribution contrast for a central circular region of 35% SO₂ and 40% SO₂ surrounding baseline. Variations are shown for waveband (586-796nm and 454-500nm) and melanosome volume fraction (light, medium, and dark skin). Scaling matches the images in figure 11. 94

Figure 5-1. Cherenkov intensity distributions at the moment of generation in tissue for 6MeV electron beamlets (left) and 6MV x-ray beamlets (right). The top of each figure is the air-tissue interface (depth = 0) with depth on the vertical axis and the horizontal axis shows the lateral distance from the center of the 1mm wide beamlet.102

Figure 5-2. Top-down views of the air-tissue surface centered at the 1x1 mm² beamlet, with insets showing the profile through the center of each corresponding plot. (left) Surface intensity contours of the emitted Cherenkov light generated by the 6MeV electron beam. (right) Cherenkov emission intensity from the surface for the 6MV x-ray beam. Both plots are normalized to the respective maximum emitted Cherenkov intensity..... 103

Figure 5-3. Emitted intensity plot of the directional distribution per unit solid angle (Sr⁻¹) of emitted light with 5 degree binning. The surface normal is designated as 90 degrees. The number of photons emitted are normalized to unity before calculating the emission per solid angle. Electron-beam-generated Cherenkov emission

(6e beam) is shown in comparison to the x-ray-generated Cherenkov emission (6x beam). 105

Figure 5-4. The photon spectral distribution of emitted light, ranging in wavelength from 350nm to 1000nm, for Cherenkov emission from tissue after generation by a 6MeV electron beam and a 6MV x-ray beam, Cherenkov emission from water after generation by the 6MV x-ray beam, and the diffusely reflected light from scatter in tissue. The plots are normalized to unit emitted photon. 107

Figure 5-5. Cherenkov surface emission distributions in the 586-796nm waveband (top row) and the 454-500nm waveband (bottom row), with 20% SO₂ in the 3cm diameter keloid lesion and 40% SO₂ baseline in the surrounding normal tissue, which the grayscale values are centered around. Variation are shown for light (2.5% melanosome volume fraction), medium (15%), and dark (40%) skin. 109

SIMULATING CHERENKOV RADIATION GENERATED BY RADIOTHERAPY BEAMS

Andy N. Wiles

Dr. Enrique W. Izaguirre & Dr. Sudarshan K. Loyalka,
Dissertation Supervisors

ABSTRACT

Cherenkov radiation has had various applications in high-energy physics since its discovery, and this research explores two applications of Cherenkov radiation relating to its presence in media under irradiation by medical radiotherapy beams. In real-time organic scintillating fiber dosimeters, the radiation fluence passing through the scintillating fibers produces Cherenkov light noise in addition to the scintillation light signal. Quantifying the Cherenkov light through Monte Carlo simulations allows us to optimize various parameters of the device, such as the spectral sensitivity profile of the photodetector attached to the end of the fiber and the fiber's shape, thickness, and emission spectrum, which allows full characterization of the Cherenkov noise in the scintillation-based detector. A second application attempts to directly measure the irradiation of surface cutaneous tissue by imaging the Cherenkov light emitted from the skin surface. The optical properties of the Cherenkov emission depend on the concentration of molecular absorbers in the epidermal and dermal layers of the skin, the optical scatter in the epidermis, and the distribution of high-energy electrons propagating through the cutaneous tissue, and the Cherenkov signal carries information on erythema development and the treatment response.

CHAPTER 1: GENERAL INTRODUCTION

I. Introduction

Real-time imaging dosimetry in external beam radiation therapy can enhance patient safety. External beam radiation therapy uses a megavoltage electron linear accelerator to produce either a scattered electron beam or a bremsstrahlung x-ray beam to treat patients. The purpose of real-time imaging dosimetry is to enhance patient safety by detecting major errors during treatment delivery and by verifying the accuracy of the treatment delivered, which is achieved by monitoring the delivered dose distribution for significant deviations from the planned dose distribution. The purpose of my research is to assess the dosimetric properties of Cherenkov radiation for external megavoltage radiation therapy applications using two real-time imaging applications.

One such method of real-time dosimetry measures the dose transmitted through organic scintillating fibers as the beam exits the linear accelerator and passes through a gantry mounted dosimeter. In organic polymer scintillating fiber optic dosimetry, ionizing electrons that cross the fiber generate scintillation light in proportion to the energy deposited within the fiber's core material, and the light output intensity is proportional to the dose deposited in the material, which is nearly water equivalent.

One potential problem with scintillating fiber dosimetry for external, megavoltage beams is the generation of Cherenkov radiation in addition to

the scintillation light. Cherenkov radiation is a continuous spectrum of low-energy, electromagnetic radiation generated in a dielectric medium by the passage of a charged particle with a velocity greater than the phase velocity of light propagating through that medium, and the amount of Cherenkov radiation produced per unit pathlength varies with the charged particle energy. In a scintillating fiber dosimeter, the passage of electrons through the organic material induces Cherenkov radiation generation in addition to the production of scintillation light. The added Cherenkov radiation distorts the relationship between dose and Cherenkov light, and accurate dosimetry requires methods to account for the Cherenkov component of the signal.

Another emerging method of real-time dosimetry in external beam megavoltage radiation therapy is the measurement of Cherenkov photons emitted directly from the patient's skin during the treatment from interactions of electrons with the skin tissue.¹ The Cherenkov light backscattered from the patient can be directly imaged with optical cameras for a variety of dosimetric or biological applications.

One technical challenge of this method is to accurately define the relationship between Cherenkov light intensity and the incident beam intensity.² Specifically of interest is the amount of Cherenkov light intensity that reaches the skin surface before being absorbed in tissue and then is subsequently emitted in a direction that can be imaged by a high resolution camera outside of the interference of the radiation beam.

The purpose of my research is to assess the properties of Cherenkov radiation involved in these two real-time imaging dosimetry applications for external beam megavoltage radiation therapy. I programmed the simulation model using Monte Carlo techniques for radiation transport into the dosimetry medium, and the simulation results allow evaluation of the imaging-related properties of each method. The first application I examined was the minimally-perturbing polymer fiber array positioned in the beam during treatment to measure the beam output spatial distribution. Then I examined the application involving Cherenkov radiation backscatter and emission from patient skin inherently induced by external beam radiotherapy.

For the first application, the objective is characterizing Cherenkov radiation produced in polymer fiber, real-time, imaging dosimeters, and the development of a model for the signal generated by the dosimeter for a given incident beam for various setup parameters. To realize this objective, I constructed a Monte Carlo program for the beam interactions in the scintillation fiber that accounts for the Cherenkov radiation produced in the fiber as well as the scintillation radiation generated. The model includes photon propagation in the fiber through to the signal at the photon detectors affixed to each end of the scintillation fiber. This model helps determine the relative contribution of Cherenkov radiation to the scintillation signal when parameters are varied. Those parameters include incident beam properties

such as energy, beam angle, field size, and modality (x-ray photons or electrons) and detector properties such as the fiber width, fiber length, fiber cross-sectional shape, scintillation spectrum, and detector spectral efficiency profile. Results of these simulations for electron beams and x-ray beams have shown the impact on scintillation light output and a metric for Cherenkov noise, the fraction of Cherenkov photons contaminating the total light output, for a variety of parameter combinations.

In the second application, the objective is the characterization of Cherenkov radiation emitted from patient skin during external beam radiation therapy. To realize this objective, I constructed a Monte Carlo program for the beam interactions in skin that lead to the production of Cherenkov photons. This model will help determine the subsequent Cherenkov photon wavelength distribution, propagation and emission from the skin surface, and the position on the skin surface, while considering the wavelength-dependent absorption by molecular absorbers and scattering by tissue structures. The backscattered Cherenkov photons from skin are compared to two cases: Cherenkov photons in water and incident optical photons backscattered from skin. Results of the simulations show the position and emission direction of Cherenkov light generated in skin as well as the wavelength distribution. These results are compared to the same properties from simulations of Cherenkov radiation in a water medium and backscatter from optical light incident on the skin medium.

II. Background

This section provides a background overview of the Cherenkov radiation effect. Explaining Cherenkov radiation in detail makes clear its distinction from other radiative effects of high energy particle travel, such as the radiation associated with atomic electrons undergoing excitation and ionization or Bremsstrahlung x-rays produced by particle acceleration near a nucleus. This overview covers the history of Cherenkov radiation, the theory and equations for it developed by Frank and Tamm, and various other applications of Cherenkov radiation.

Mallet observed Cherenkov radiation in 1926, in advance of the discovery by Vavilov and Cherenkov in 1934, but did not continue with the work beyond 1929 and assumed it was a type of fluorescence.³ Mallet observed bluish white light from a gamma-ray source placed in water, and measurements taken with film showed over a five-fold increase in darkening of the film relative to the exposure directly caused by the gamma-ray source. Furthermore, the radiation was found to mostly have short wavelengths by comparing the intensity after filtering with glass, which absorbs most photons of shorter wavelength than near-ultraviolet, compared to the intensity after filtering with quartz, which is transparent to ultraviolet light. Mallet's additional spectral measurements from the years 1928 to 1929 showed that the radiation was continuous and that it extends continuously

up to wavelengths of 436 nm, the upper limit of the spectral measurements performed.

Vavilov and Cherenkov are credited with discovering the Cherenkov radiation effect, also called Vavilov-Cherenkov radiation, in 1934. After initially working with luminescence of salts in solution, Cherenkov found that gamma-ray radiation could also induce pure solvents to emit light.⁴ The observed glow was attributed to a new physical effect, rather than to luminescence, because they found no detectable excitation lifetime after a series of quenching experiments that are typically used to measure the excitation lifetimes of luminescent materials. Experiments with an applied magnetic field and beta particles showed that the radiative glow was caused by electrons traversing the solvent and that the intensity depended upon the electron beam direction. From those experiments, the presence of anisotropy in the intensity distribution of the electromagnetic waves led Frank and Tamm to develop a theory for the observed effect based upon the Huygens principle for propagation of wave fronts.

In 1937 Frank and Tamm developed the theory for Cherenkov radiation, which provides results that change very little, when later on, higher order terms were included based on quantum theory.³ From the original theory, the equation for Cherenkov radiation output as electromagnetic energy W per unit time is

$$\frac{dW}{dt} = \frac{e^2}{c^2} \int \left(1 - \frac{1}{\beta^2 n^2}\right) \omega d\omega$$

where e is the electric charge, c is the vacuum speed of light, βc is the electron speed, $\omega = 2\pi\nu$ for the frequency, and $n(\omega)$ is the refractive index of the medium. There is a threshold for Cherenkov production that requires that the refractive index $n(\omega) > 1/\beta$, which typically restricts the spectrum to ultraviolet, visible, and infrared wavelengths for transparent media. The equation can be expressed in terms of the number of photons N emitted per unit pathlength r by changing ω to units of wavelength λ and taking the energy per photon as hc/λ such that $W = N hc/\lambda$ and integrating over a spectral range from λ_1 to λ_2 in which $n(\omega)$ is approximately constant. The resulting equation is

$$\frac{dN}{dr} = 2\pi \alpha \left(\frac{1}{\lambda_2} - \frac{1}{\lambda_1} \right) \left(1 - \frac{1}{\beta^2 n^2} \right)$$

where $\alpha = e^2/(2\pi hc) \approx 1/137$ is the fine structure constant.

The number of photons per unit wavelength interval varies proportionally to the inverse wavelength squared, for values of $n(\omega)$ that are approximately constant. This explains the typically bluish-white appearance of Cherenkov radiation generated by charged particles traversing water and other transparent media. As wavelengths go into the far-ultraviolet the value of $n(\omega)$ approaches 1 and the number of Cherenkov photons tends to vanish due to the $(1 - 1/\beta^2 n^2)$ term and the threshold $\beta > 1/n$. Thus, for most transparent media, the spectral characteristics of Cherenkov radiation fall into the near-ultraviolet and visible spectrum because the spectral

distribution is bounded at short wavelengths by the change in $n(\omega)$ and at long wavelengths by the $dN/d\lambda \propto 1/\lambda^2$ relationship.

The Cherenkov relation for the emission angle relative to the particle track,

$$\cos \theta = \frac{1}{\beta n}$$

depends only on n the index of refraction and the particle velocity βc , and the emission is symmetric about the azimuth of the axis formed by the particle path. The minimum velocity threshold for production of Cherenkov radiation, when expressing the speed as relative to c , is

$$\beta_{\min} = \frac{1}{n}$$

where the emission angle goes to zero. The maximum emission angle occurs as $\beta \rightarrow 1$ at an angle of $\theta_{\max} = \cos^{-1}(1/n)$.

A variety of experimental applications using measurement of Cherenkov radiation have existed since the beginning of the 1950s shortly after Cherenkov counters were proposed following the development of photomultiplier tubes.^{3, 4} Cherenkov counters consist of a radiator that produces Cherenkov radiation from a charged particle passing through it and an optically coupled photomultiplier tube that receives the Cherenkov radiation and produces a signal.⁴ In contrast to Geiger counters, Cherenkov counters do not have dead-time because the light is generated and propagates directly to the photomultiplier tube, and the two components of the Cherenkov counter can be optically coupled in such a way that the direction

of the detected particle can be determined. In 1951 Cherenkov counters were first used to detect single, high-energy, charged particles, followed in the same year by the direct measurement of the particle velocity of high-energy accelerator beams, and later in 1955 Cherenkov detectors were involved in discovering the anti-proton.³ The requirement of charged particles exceeding a threshold speed does limit Cherenkov counters to only certain applications though, such as in high energy physics experiments that measure single particle interactions in large water tanks like muon production and neutrino interactions.⁴ However, applications of Cherenkov radiation detection are not limited to just Cherenkov counters. An example is in measuring atmospheric cosmic-ray showers, where cosmic radiation entering the atmosphere results in ionization of the gases in the atmosphere.⁴ The electrons generated by atmospheric ionization produce Cherenkov radiation at radiofrequencies, which allows remote observation of electromagnetic showers at radio-astronomy stations. Those are a few of the long existing applications of Cherenkov radiation, and this dissertation will look at two recent applications in the form of Cherenkov radiation generated by megavoltage radiotherapy beams.

III. Thesis Organization

A brief outline of the remaining chapters in this dissertation follows.

- Chapter 2 is a literature review. It is divided into two sections: first, a review of scintillation fiber applications in medical physics, then a review of Cherenkov imaging in medical physics.
- Chapter 3 covers the Monte Carlo simulations of the scintillating fiber detector. This chapter is entirely self-contained as a paper and follows the formatting of a manuscript for the Medical Physics journal.
- Chapter 4 moves on to simulations of Cherenkov emission from cutaneous tissue, and this chapter is also a self-contained article that also follows the same manuscript formatting as Chapter 3.
- Chapter 5 appends additional results for Cherenkov emission from cutaneous tissue. The chapter focuses on simulations of an incident beam of electrons with comparisons to the Cherenkov emission that results from an incident x-ray beam.
- Chapter 6 concludes the dissertation in general with a discussion of the results and recommendations for future research.

IV. References

- ¹ L.A. Jarvis, R. Zhang, D.J. Gladstone, S. Jiang, W. Hitchcock, O.D. Friedman, A.K. Glaser, M. Jermyn, B.W. Pogue, "Cherenkov video imaging allows for the first visualization of radiation therapy in real time," *International journal of radiation oncology, biology, physics* **89**, 615-622 (2014).
- ² A.K. Glaser, R. Zhang, D.J. Gladstone, B.W. Pogue, "Optical dosimetry of radiotherapy beams using Cherenkov radiation: the relationship between light emission and dose," *Physics in medicine and biology* **59**, 3789-3811 (2014).

- ³ J.V. Jelley, *Cerenkov radiation : and its applications*. (Pergamon Press, New York, 1958).
- ⁴ B.M. Bolotovskii, "Vavilov – Cherenkov radiation: its discovery and application," *Physics-Uspeski* **52**, 1099-1110 (2009).

CHAPTER 2: LITERATURE REVIEW

I. Scintillation fibers

Plastic scintillation dosimetry uses the scintillation light, corresponding to dose received in the scintillator, to determine the dose delivered to a medium, and an early setup used simple plastic scintillation blocks optically coupled to an optical fiber to transmit the signal to a photodetector outside of the radiation field¹⁻³, which had the inherent problem of also collecting Cherenkov radiation generated in the optic fiber inside the radiation field. The advantage of plastic scintillators are that they are water equivalent, having very similar atomic composition, density, and electron density to water.³ Furthermore, the small size and water equivalence of the scintillator means that its presence in a water medium does not perturb the radiation beam passing through the plastic scintillator, making it ideal for radiotherapy QA dosimetry where measurements are made at depths in water.

Burlin cavity theory predictions of the scintillator/water dose ratio were experimentally tested and confirmed for radiotherapy beams, measured at 13 MeV to 19 MeV by Clift et al⁴, with the scintillator/water dose ratio measured as 0.962 +/- 0.008 in that energy range compared to the theoretical prediction of 0.963 +/- 0.002. The results confirmed that the scintillator detectors would be water equivalent for megavoltage photon beams, and only a single

correction factor would be required for dosimetry measurement based on a calibration of the detector.

Dealing with Cherenkov radiation was approached in several ways. Clift et al⁵ used techniques to minimize the Cherenkov contribution to the signal by using scintillators with reflective coating to amplify the signal, long-wavelength shifted scintillators to separate the signal from the short-wavelength Cherenkov contamination, and absorbers to selectively absorb light with wavelengths outside of the scintillation emission spectrum. Fontbonne et al⁶ developed a method using spectral differences between Cherenkov light and the scintillation light and separate the green and blue components of the signal from a single scintillating fiber to determine the scintillation signal by comparing the measured channel ratio to a calibrated channel ratio, with accuracy within 1% of the expected dose. A method used by Lambert et al⁷ removed the Cherenkov signal by employing an air-core optical fiber – a plastic clad core of air, which does not generate Cherenkov photons – for the in-field portion of the fiber. The drawback of an air-core optical fiber is that the Cherenkov photons are highly attenuated when passing through that portion of the fiber. While the contaminating Cherenkov light found in solid-core optical fibers was not generated, the signal from the plastic scintillator was extremely attenuated.

Scintillating fiber arrays, replacing the optical fiber and scintillator block with a scintillator doped optical fiber, has been studied by several

researchers⁸⁻¹⁵, but no solution to account for the Cherenkov component of the signal has allowed real time evaluation of the dosimetric measurement with high spatial resolution. The existing research in this field relies on CCD detectors that require extensive time to process the data or else a detector setup requiring an undoped optical fiber to collect Cherenkov radiation for background subtraction, resulting in the loss of spatial resolution. Other dosimeter types, using ion chamber arrays¹⁶, are able to monitor the dose during delivery but lack the ability to resolve the spatial distribution of the delivered radiation beam that a scintillating fiber array has the ability to do. A similar system that uses scintillating fibers instead of ionization chambers was developed by Lamanna *et al*¹⁷, who developed a detector prototype using a closely-packed array of scintillating fibers as a 2D homogeneous sheet to image a plane of the beam in real-time, but the resolution was limited to the size of the photodiodes used, which causes large artifacts in the image of non-rectangular fields.

Our research group has developed a prototype high resolution real time scintillating fiber detector¹⁸ that allows us to determine in real time the accuracy of stereotactic radiosurgery (SRS) and stereotactic body radiotherapy (SBRT) treatments by attaching in transmission mode at the output port of a micro-MLC, with the motivation of enhancing dose delivery accuracy and to achieve error free radiosurgery. A high-density array of scintillating fibers with a pitch of 0.5 mm and a high-speed photo detector

array with readout speed of 1.2 msec and 0.5 usec response time were integrated to implement a high resolution real time dosimeter that can sample pulsed SRS and SBRT beams cross sections. The high efficiency of the developed system allows reading each linac pulse in real time and computing the accumulated dose and dose errors smaller than 3% when less than 1/100th of the beam is delivered.

A second prototype our group developed¹⁹ of the in vivo transmission scintillation fiber detector was developed utilizing a set of 60 parallel scintillating fibers that were coupled to match the multi-leaf collimator (MLC) leaf pairs so that the beam fluence between each leaf-pair could be monitored in real time. The detector system is for large fields and can be mounted in the accessory tray of a linac gantry head, and the scintillating fibers are long enough to capture a projected 40 cm wide field. The detector was found to respond linearly with dose, independently of beam energy, and independent of the dose rate, while the polymer substrate the fibers are embedded in attenuates only 2.65% of the beam. Real time in vivo beam monitoring is possible with this system to enhance patient safety and treatment delivery accuracy by detecting dose errors from each MLC leaf pair.

A third prototype variation of the in vivo transmission scintillation fiber detector²⁰ was designed for standard-MLC-based SBRT and cone-based SRS real time treatment delivery monitoring with the system being mounted in

the linac accessory tray. A set of two high-density scintillating fiber linear arrays are layered to form an X-Y grid and captures the linac pulses in real time during treatment delivery while the detector rotates through 360 degrees to capture angular beam projections. The reconstructed beam profiles are produced in real-time with sub-millimeter spatial resolution and 1% dose output resolution. This detector system has the ability to detect dosimetric errors of less than 1%, allowing SBRT and SRS treatments to be delivered error free.

II. Cherenkov imaging in tissue

High energy electrons traveling through any dielectric medium, including human tissue, will generate Cherenkov radiation. The theoretical relationship between radiation dose and Cherenkov radiation emission should ideally be constant with the energy of the particle, and one study of this used analytic and Monte Carlo methods to relate Cherenkov photon generation position and dose deposition position for various radiation beam sizes, modalities (bremsstrahlung, Co-60, and electron beams), and energies.²² Cherenkov radiation generation per volume element was found to be predictive of dose deposited in that element. However, as indicated by the study's authors, although they scored the positions in the Monte Carlo simulations, the directionality of the Cherenkov photon was not considered. Since the Cherenkov radiation emission direction is anisotropic, Cherenkov radiation visualization is angle dependent. The study was not able to

establish the relationship between visualization of the resulting Cherenkov radiation in a particular location to the absolute dose deposited in that location. However, if the anisotropy can be removed the Cherenkov radiation would theoretically predict the dose and allow visualization of the dose in real time.

Anisotropy was effectively removed from Cherenkov radiation in a study using a water tank with a fluorescent dye doping the water, which absorbed the Cherenkov radiation and undergoes isotropic re-emission, and treatment plan quality assessment using Cherenkov radiation optical dosimetry was shown to be feasible with the water tank and a CCD camera.²³ In that study the authors focused on relative dosimetry of dynamic IMRT and VMAT treatment plans where superposition of parallel opposed beams mitigates the variations in the energy fluence spectrum with depth that results in disproportionality between absorbed dose and the Cherenkov photon generation with depth. To counter the anisotropic emission of Cherenkov radiation, the water tank was doped with a fluorescent dye to absorb the Cherenkov radiation and re-emit isotropic light. The resulting image sets were summed to visualize the full beam over the entire rotational treatment. The summed Cherenkov image was found to match the intensity of the planned dose distribution when projected into the same viewing plane.

In contrast to the treatment plan quality assurance methods described previously, another recent study used pulsed CCD imaging of Cherenkov

radiation surface emissions from patient skin during radiation therapy for real time visualization of the beam modulation and positioning.²⁴ That study correlated high intensity Cherenkov emission locations to excessive dose hot spots on the skin surface that resulted in patient skin reactions, indicating that the method is successfully able to use the Cherenkov light intensity emitted from patient skin to predict the skin surface dose. The authors also noted that the visualization of major arteries in the images, caused by absorption of the Cherenkov photons passing through the vasculature, allows the possibility of checking patient positioning to within 1 to 2 mm over the course of the treatment. This study would indicate that the technique feasibly could perform relative dosimetry in vivo and during treatment. However, absolute dosimetry using the Cherenkov emissions at the superficial surface has yet to be achieved, which would require modeling the optical interactions in skin to account for the anisotropic emission of Cherenkov radiation.

An evaluation of the concept of Cherenkov imaging for patient positioning validation and movement tracking took place in a phase 1 clinical trial.²⁵ During each treatment fraction a set of Cherenkov images were obtained, and this was done for several separate treatment fractions for each patient, and the sets were then analyzed. Positioning validation for inter-fraction setup error was done by comparing the beam-edge apparent on the Cherenkov images from each individual fraction to the average of the set of images over the whole treatment, and blood vessels that appeared in the images also

served as markers for the image registration algorithm. Retrospective movement tracking of respiratory motion matched each frame of the image set in a fraction to the average, thereby providing a measure of the amplitude of patient motion during the treatment. The results were consistent with the expected values, and they further found that the blood vessel visualization showed volume deformations in the treatment region, suggesting an application of Cherenkov imaging in deformable image registration.

In terms of modeling the light transport through tissue, one example of a methodology is the Kubelka-Munk method.^{26, 27} The Kubelka-Munk method would specifically model the light incident on skin and account for subsequent interactions throughout different layers that ultimately scatter back out of the skin. For external beams of optical radiation, as assumed in the Kubelka-Munk model, the light source is entirely external from the patient skin. This will not work well in our case because the passage of high-energy electrons generates optical light throughout the entire volume of skin rather than starting with a source plane at the skin surface.

A model that accounts for the three-dimensional source with anisotropic scattering and a continuous wavelength distribution in a material with wavelength-dependent optical properties may best be solved using Monte Carlo techniques. There are numerous sources of semi-empirical and experimentally derived data of optical properties of skin and muscle tissues, and a recent review article²⁸ included a collection of data from many sources.

One example of a three-dimensional Monte Carlo algorithm, Monte Carlo Simulations using Voxel Library (MCSVL),²⁹ uses a wavelength-dependent optical property library in a voxel-based simulation in the trans-illumination imaging of skin lesions. The trans-illumination uses a ring light source against the skin surrounding the region of interest that transversely scatters through the skin before being reflected out for imaging at the site of the lesion. While most simulations assume that skin consists of layers where each layer has homogeneous properties, the MCSVL algorithm uses voxel-based optical properties to represent the nonhomogeneous tissue structures that are difficult to model using mathematical equations for the irregular shapes found in skin surface lesions.

Since the focus of this research is to characterize the Cherenkov radiation emitted from skin tissue as the beam enters the skin, a simple model of homogeneous layers can be used. Monte Carlo simulations in this research are based on optical propagation techniques in homogeneous layers of skin tissue as developed by Prahl et al³⁰ and using optical properties summarized in a review by Jacques.³¹ Therapeutic laser treatment of superficial tumors by heating motivated the literature in this area. While their works focused on a beam incident on the skin surface and the thermal effects throughout the tissue, the converse is applicable to this research, where we are interested in light generated throughout the tissue that is ultimately emitted from the surface back into the air.

III. References

- 1 A.S. Beddar, K.J. Kinsella, A. Ikhlef, C.H. Sibata, "A miniature "scintillator-fiberoptic-PMT" detector system for the dosimetry of small fields in stereotactic radiosurgery," *IEEE Transactions on Nuclear Science* **48**, 924-928 (2001).
- 2 A.S. Beddar, T.R. Mackie, F.H. Attix, "Water-equivalent plastic scintillation detectors for high-energy beam dosimetry: II. Properties and measurements," *Physics in medicine and biology* **37**, 1901-1913 (1992).
- 3 A.S. Beddar, T.R. Mackie, F.H. Attix, "Water-equivalent plastic scintillation detectors for high-energy beam dosimetry: I. Physical characteristics and theoretical consideration," *Physics in medicine and biology* **37**, 1883-1900 (1992).
- 4 M.A. Clift, R.A. Sutton, D.V. Webb, "Water equivalence of plastic organic scintillators in megavoltage radiotherapy bremsstrahlung beams," *Physics in medicine and biology* **45**, 1885-1895 (2000).
- 5 M.A. Clift, R.A. Sutton, D.V. Webb, "Dealing with Cerenkov radiation generated in organic scintillator dosimeters by bremsstrahlung beams," *Physics in medicine and biology* **45**, 1165-1182 (2000).
- 6 G.I. J. M. Fontbonne, G. Ban, A. Battala, J. C. Vernhes, J. Tillier, N. Bellaize, C. Le Brun, B. Tamain, K. Mercier, and J. C. Motin, "Scintillating Fiber Dosimeter for Radiation Therapy Accelerator," *IEEE TRANSACTIONS ON NUCLEAR SCIENCE* **49**, 2223-2227 (2002).
- 7 J. Lambert, Y. Yin, D.R. McKenzie, S.H. Law, A. Ralston, N. Suchowerska, "A prototype scintillation dosimeter customized for small and dynamic megavoltage radiation fields," *Physics in medicine and biology* **55**, 1115-1126 (2010).
- 8 L. Archambault, J. Arsenault, L. Gingras, A. Sam Beddar, R. Roy, L. Beaulieu, "Plastic scintillation dosimetry: Optimal selection of scintillating fibers and scintillators," *Medical Physics* **32**, 2271 (2005).
- 9 G. Bartesaghi, V. Conti, D. Bolognini, S. Grigioni, V. Mascagna, M. Prest, S. Scazzi, A. Mozzanica, P. Cappelletti, M. Frigerio, S. Gelosa, A. Monti, A. Ostinelli, G. Giannini, E. Vallazza, "A scintillating fiber dosimeter for radiotherapy," *Nuclear Instruments and Methods in*

Physics Research Section A: Accelerators, Spectrometers, Detectors and Associated Equipment **581**, 80-83 (2007).

- 10 M. Goulet, L. Archambault, L. Beaulieu, L. Gingras, "High resolution 2D dose measurement device based on a few long scintillating fibers and tomographic reconstruction," *Med Phys* **39**, 4840-4849 (2012).
- 11 M. Goulet, L. Archambault, L. Beaulieu, L. Gingras, "3D tomodosimetry using long scintillating fibers: a feasibility study," *Med Phys* **40**, 101703 (2013).
- 12 M. Goulet, L. Gingras, L. Beaulieu, "Real-time verification of multileaf collimator-driven radiotherapy using a novel optical attenuation-based fluence monitor," *Medical Physics* **38**, 1459 (2011).
- 13 F.d. Lacroix, L. Archambault, L. Gingras, M. Guillot, A.S. Beddar, L. Beaulieu, "Clinical prototype of a plastic water-equivalent scintillating fiber dosimeter array for QA applications," *Medical Physics* **35**, 3682 (2008).
- 14 B. Lee, K.W. Jang, D.H. Cho, W.J. Yoo, H.S. Kim, S.-C. Chung, J.H. Yi, "Development of One-dimensional Fiber-Optic Radiation Sensor for Measuring Dose Distributions of High Energy Photon Beams," *Optical Review* **14**, 351-354 (2007).
- 15 B. Lee, K.W. Jang, D.H. Cho, W.J. Yoo, G.-R. Tack, S.-C. Chung, S. Kim, H. Cho, "Measurements and elimination of Cherenkov light in fiber-optic scintillating detector for electron beam therapy dosimetry," *Nuclear Instruments and Methods in Physics Research Section A: Accelerators, Spectrometers, Detectors and Associated Equipment* **579**, 344-348 (2007).
- 16 J. Chang, R.K. Heaton, R. Mahon, B.D. Norrlinger, D.A. Jaffray, Y.B. Cho, M.K. Islam, "A method for online verification of adapted fields using an independent dose monitor," *Med Phys* **40**, 072104 (2013).
- 17 E. Lamanna, A.S. Fiorillo, A. Gallo, A. Trapasso, R. Caroleo, R. Brancaccio, G. Barca, S. Carnevale, F. Castrovillari, Y.F.T. Siaka, "Dosimetric Study of Therapeutic Beams Using a Homogeneous Scintillating Fiber Layer," *IEEE Transactions on Nuclear Science* **60**, 109-114 (2013).
- 18 E. Izaguirre, S. Price, T. Knewton, S. Loyalka, D. Rangaraj, "TU-F-BRE-01: A High Resolution Micro Fiber Scintillator Detector

- Optimized for SRS and SBRT in Vivo Real Time Treatment Verification," *Medical Physics* **41**, 468-468 (2014).
- 19 T. Knewton, S. Pokhrel, D. Hernandez-Morales, S. Price, S. Loyalka, D. Rangaraj, E. Izaguirre, "WE-AB-BRB-09: Real Time In Vivo Scintillating Fiber Array Detector for Medical LINACS," *Medical Physics* **42**, 3651-3651 (2015).
- 20 T. Knewton, S. Pokhrel, S. Loyalka, E. Izaguirre, "SU-F-T-559: High-Resolution Scintillating Fiber Array for In-Vivo Real-Time SRS and SBRT Patient QA," *Medical Physics* **43**, 3591-3592 (2016).
- 21 Y. Yin, J. Lambert, S. Yang, D.R. McKenzie, M. Jackson, N. Suchowerska, "A self-checking fiber optic dosimeter for monitoring common errors in brachytherapy applications," *Medical Physics* **36**, 2985 (2009).
- 22 A.K. Glaser, R. Zhang, D.J. Gladstone, B.W. Pogue, "Optical dosimetry of radiotherapy beams using Cherenkov radiation: the relationship between light emission and dose," *Physics in medicine and biology* **59**, 3789-3811 (2014).
- 23 A.K. Glaser, J.M. Andreozzi, S.C. Davis, R. Zhang, B.W. Pogue, C.J. Fox, D.J. Gladstone, "Video-rate optical dosimetry and dynamic visualization of IMRT and VMAT treatment plans in water using Cherenkov radiation," *Med Phys* **41**, 062102 (2014).
- 24 L.A. Jarvis, R. Zhang, D.J. Gladstone, S. Jiang, W. Hitchcock, O.D. Friedman, A.K. Glaser, M. Jermyn, B.W. Pogue, "Cherenkov video imaging allows for the first visualization of radiation therapy in real time," *International journal of radiation oncology, biology, physics* **89**, 615-622 (2014).
- 25 R. Zhang, J.M. Andreozzi, D.J. Gladstone, W.L. Hitchcock, A.K. Glaser, S. Jiang, B.W. Pogue, L.A. Jarvis, "Cherenkovoscopy based patient positioning validation and movement tracking during post-lumpectomy whole breast radiation therapy," *Physics in medicine and biology* **60**, L1-14 (2015).
- 26 R.R. Anderson, J.A. Parrish, "The Optics of Human Skin," *Journal of Investigative Dermatology* **77**, 13-19 (1981).

- ²⁷ E. Claridge, S. Cotton, P. Hall, M. Moncrieff, "From colour to tissue histology: Physics-based interpretation of images of pigmented skin lesions," *Medical Image Analysis* **7**, 489-502 (2003).
- ²⁸ A.N. Bashkatov, E.A. Genina, V.V. Tuchin, "OPTICAL PROPERTIES OF SKIN, SUBCUTANEOUS, AND MUSCLE TISSUES: A REVIEW," *Journal of Innovative Optical Health Sciences* **04**, 9-38 (2011).
- ²⁹ S.V. Patwardhan, A.P. Dhawan, P.A. Relue, "Monte Carlo simulation of light-tissue interaction: three-dimensional simulation for trans-illumination-based imaging of skin lesions," *IEEE transactions on biomedical engineering* **52**, 1227-1236 (2005).
- ³⁰ S.A. Prahl, M. Keijzer, S.L. Jacques, A.J. Welch, "A Monte Carlo Model of Light Propagation in Tissue," 1989).
- ³¹ S.L. Jacques, "Corrigendum: Optical properties of biological tissues: a review," *Physics in medicine and biology* **58**, 5007-5008 (2013).

CHAPTER 3: Contribution of Cherenkov radiation in scintillator fiber detectors

Purpose: To quantify and predict the Cherenkov radiation produced inside plastic scintillating optical fiber dosimeters used in real-time, in vivo dosimetry of clinical radiotherapy beams.

Methods: We developed a Monte Carlo algorithm to model polymer scintillating fiber fluorescence and Cherenkov emission when irradiated with megavoltage radiotherapy beams. The model accounts photon generation cross-sections, wavelength-sampling, optical capture at the core-cladding interface, and transport efficiency through the fiber by incorporating indices of refraction, optical attenuation spectra, and the fiber geometry and dimensions. We study the Cherenkov emission dependency on dosimeter's fiber cross section dimensions, shape, scintillation emission spectrum, characteristic spectral sensitivity profiles of a SiPM and a photodiode detector, incident beam's energy, ionizing radiation modality (photons or electrons), and relative orientation between fiber and ionizing radiation.

Results: Cherenkov radiation outside of the wavelength range of the scintillation spectrum but falling within the spectral sensitivity range of the photodetector contributed a substantial amount of Cherenkov to the total signal; 61% and 67% of the total Cherenkov emission is detected by a photodiode fell outside of the BCF-12 and BCF-60 scintillation spectra,

respectively. We found square fibers capture 1% as much of the generated Cherenkov light as scintillation light at the fiber cladding interface for a normally incident 6 MeV electron beam compared to 37% with round fibers. Decreasing the fiber width below approximately 1x1 mm began to decrease the transmission efficiency, losing 8% of scintillation light at 0.5x0.5 mm and an additional 15% at 0.25x0.25 mm, while larger fiber widths would reduce the spatial resolution of the system.

Conclusions: Our analysis of the results suggests an optimal scintillating fiber dosimeter require a photodiode with optical filtering restricted to the emission wavelength range, using a green-shifted fiber such as the BCF-60 square fiber with edge width near 1x1 mm. For a normally incident photon beam, the system will produce approximately 1% Cherenkov radiation in the signal, and additional optical filtering may reduce that to 0.33%.

I. Introduction

Plastic scintillators are excellent dosimeters with water equivalent dose response, energy-independent response, and no polarization or density effect.¹⁻³ The general configuration of a fiber scintillator dosimeter active sensor consists of a plastic scintillating fiber attached to a non-scintillating optical fiber to transmit the light to a photodetector placed outside of the radiation field and the signal processing electronics. Single sensors or array of sensor are typically used for clinical photon and electron beam dosimetry.

In a fiber sensor, Cherenkov radiation is generated in the scintillating and non-scintillating fiber exposed to the ionization radiation, and it will propagate through the fiber which will add spurious signal to the sensor output which is not proportional to the delivered dose. Cherenkov photons do not reflect the true energy deposition in the optical fiber because only a portion of the measured beam secondary electrons has energy greater than the Cherenkov production threshold.

Consequently, correction of the output to separate Cherenkov's radiation from the scintillating emission is required to achieve accurate dosimetry in high energy clinical beams. Several methods have been developed to reject Cherenkov light contamination.⁴⁻⁷ A common correction method is to subtract the blue Cherenkov component from the signal by determining this emission from a second, parallel non-scintillating optical fiber.¹ While the plastic scintillating fiber-optic detector has excellent spatial resolution and is shown to be appropriate for small field dosimetry,⁸ the requirement of a second parallel fiber limits the practical scope of the optical fiber dosimeters to low gradient fields and adds great complexity to the design and implementation of fiber arrays such as arrays matched to the linac MLC leaves for real time dosimetry and in vivo treatment error detection.^{9, 10}

To improve upon the design, various techniques can minimize the Cherenkov contribution such as using long-wavelength emitting scintillators to spectrally separate the signal from the short-wavelength Cherenkov

emission and using optical filters to selectively absorb light outside of the scintillation emission spectrum.^{11, 12} These considerations reduce the impact of Cherenkov radiation on dose measurement accuracy but do not eliminate the Cherenkov signal completely. However, the Cherenkov photons will produce an almost constant component across all the scintillating center emission which can be eliminated using electronic thresholding¹³.

The general conclusion of the previous work is an analysis of the factors affecting the scintillation and Cherenkov signal generated and transmitted in a doped or non-doped fiber is a key element in the design of dosimeters based in scintillating fiber sensors. Results by Lee *et al*¹⁴ and Jang *et al*¹⁵ quantify the Cherenkov radiation generated in scintillation fibers by electron beams as a function of beam angle, beam energy, and field size. Those results show a maximum Cherenkov contribution at a certain beam angle that falls off to zero at normally incident angles, although these results only hold for electron beams.

Through modeling and simulation, here we expand the scope of the mentioned authors work to examine the role of several factors in the design of scintillating fiber sensors, such as the fiber's scintillation emission spectrum, cross section dimensions, shape, active length; the ionizing radiation's energy, modality (photons or electrons), and relative orientation of the fiber with respect to the ionization radiation beam; and the photodetector's spectral sensitivity profiles and efficiency, that influence the signal from

organic scintillating fibers. The product of this study is to provide a guide for development scintillating fiber detectors capable of real time transmission detection of linac output with accurate dosimetry by controlling the Cherenkov photons.

In our model and simulations, we follow the propagation vector of the linac and account for the Cherenkov component arising from each pulse, allowing real time dosimetry of the beam output without the loss of resolution occurring in the subtraction method or the loss of real-time detection occurring in methods requiring data post-processing. These results provide insights into role of the various factors that would aid in the design and development of improved detection systems.

Megavoltage electrons passing through the interface between an organic optical fiber sensor and air will generate Cherenkov radiation in the optical range and a fraction of it will be trapped in the fiber and propagate though it until it reaches the detector. In a fiber is doped with a scintillating dye molecule, electrons will generate a scintillation signal proportional to their energy loss and this effect which is linear with the dose delivered is used to detect and measure radiation beams dose deposition. The Cherenkov radiation spectrum is continuous and its photon distribution per unit of wavelength is inversely related to the wavelength squared. Therefore, the number of photons increases as the wavelength decreases giving Cherenkov radiation the characteristic blue that spans from the deep blue to the

scintillation center emission spectrum and across the visible spectrum of light.

II. Methods

II.A. Cherenkov emission characteristics

Cherenkov photons are emitted when a charged particle (electrons) travels through a dielectric medium faster than the phase velocity of light, which is the ratio of the speed of light in vacuum, c , to the refractive index, n , of the medium. The emission threshold in terms of the electron's relative velocity is $\beta_{min} = v_{min}/c = 1/n$, which is related to the kinetic energy, T , through the equation,

$$\beta = \sqrt{1 - \frac{1}{\left(\frac{T}{mc^2} + 1\right)^2}}, \quad 1$$

and the kinetic energy threshold for Cherenkov radiation emission is found by relating the kinetic energy to its speed through the Lorentz factor as follows in Equation 2,

$$T_{min} = mc^2 \left(\frac{1}{\sqrt{1-n^{-2}}} - 1 \right). \quad 2$$

A charged particle emits Cherenkov radiation only at a particular cone defined by the angle θ_p respect to the electron's path,

$$\cos\theta_p = (n\beta)^{-1}. \quad 3$$

For a given medium with index of refraction n , the relative emission angle

depends only on the electron energy through the relativistic velocity β . Electrons with energies near the production threshold will emit forward directed Cherenkov photons, while at increasing energies ($\beta \rightarrow 1$) the emission angle will approach a maximum defined by the arc-cosine of the inverse of the refractive index where the charged particle is propagating.

II.B. Physics and geometry of the formulated Cherenkov emission and propagation model

We model a mono-energetic beam of either x-rays or electrons incident on an organic polymer scintillating fiber embedded between a pair of 3 mm thick plates of acrylic (figure 1). For a beam of x-rays, interactions in the materials produce secondary electrons; for a beam of electrons, interactions begin upon entering the surface of the acrylic plate; and, in both cases, the same model is used for electron propagation inside the acrylic plate and fiber volume. Electrons, primary or secondary, interacting with the scintillating fiber generate both scintillation photons and Cherenkov photons. An optical photon's propagation vector determines if the photon will undergo total internal reflection in the interface between the fiber core and shaft coating or will escape the fiber. For each captured photon, we compute the weight fraction surviving fiber core inherent absorption and the weight fraction detected by either of the photodetectors placed at the fiber ends.

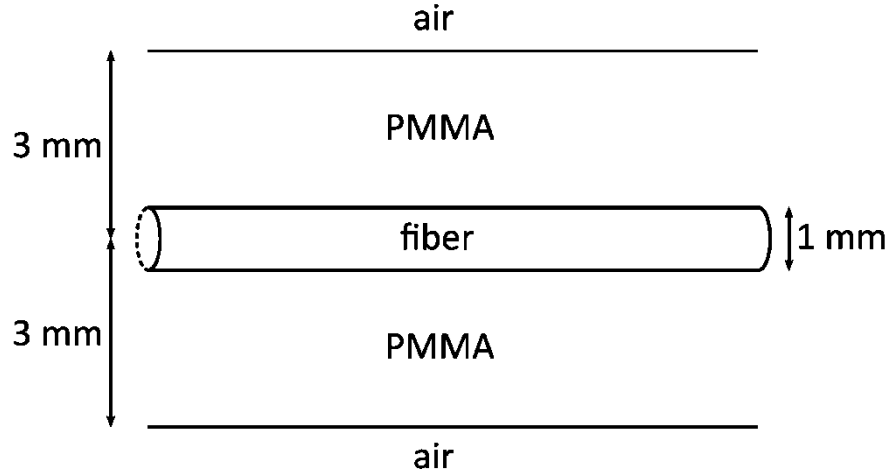


Figure 3-1: Diagram of the detector containing a round scintillation fiber embedded between two plates of acrylic.

The developed model has several input parameters such as the scintillating fiber diameter for circular and side for square cross sections, fiber active length, and scintillator emission spectra. We model two photo-detector technologies, a photodiode with a peak quantum yield of 0.9 electrons per photon at 850nm and a silicon photomultiplier (SiPM) with a photon detection efficiency of 48% at 450nm. The incident beam source is modeled as a point source with a variable distance and orientation relative to the fiber. Algorithm input arguments allow varying the intersection point of the beam on the fiber and the fiber irradiated length, the primary beam particle, and the nominal beam energy.

Each simulated primary particle propagation vector is randomly sampled from the permissible vectors defined by each input parameter's range to create a divergent beam. For an electron beam, each electron starts at the intersection point of the initial propagation vector and the top plane of the acrylic plate. For an x-ray beam, the mean free path of x-rays is large compared to the depth of the acrylic plate, so we improve simulation efficiency with forced interactions within the detector volume to only model the subset of x-ray interactions occurring within the plate with a statistical probability proportional to the photon track length intersection with the fixed geometry of the acrylic plate and polystyrene fiber core. Random sampling along this restricted track length determines the interaction site, and the statistical weight is passed down to the subsequently generated secondary electrons and the Cherenkov and scintillation photons arising from those electrons. We sample Compton electron emission angle from the Klein-Nishina cross-sections, and we sample the photoelectron angle from a uniform isotropic distribution under the assumption that inaccuracies for photoelectrons are negligible for our overall results given the low probability of photoelectric interactions in the energy range of interest.

The electron traverses the fiber through a series of interactions which are randomly modeled using the interaction probabilities for Cherenkov, soft collisional energy loss, and Coulomb scattering interaction events. Each interaction defines the electron path vector to the new position, and the

energy loss is simulated according to the rate of energy deposition according to the type of interaction. The free path lengths are small enough to assure a simulation equivalent to the continuous approximation. Electrons stops are ended when they escape from the acrylic plate or the electron's energy is null. For electrons inside the fiber, Cherenkov photon or scintillation photons are generated according to the type of interaction which is determined by the sampling probability of these competing effects.

We model continuous energy loss as the electron propagates through the medium with collisional stopping power data from the NIST ESTAR database. We model Coulomb scattering differential cross section using

$$\frac{d\sigma_e}{d\Omega_e} = \left(\frac{Zke^2}{2\beta^2(T+mc^2)} \right)^2 \left[\csc^4\left(\frac{\theta_e}{2}\right) - \beta^2 \csc\left(\frac{\theta_e}{2}\right) \right]. \quad 4$$

This equation assumes the conditions for the Mott-Born approximation for a point nucleus with no shielding¹⁶ and is valid for energies above 0.036 MeV and scattering angles larger than 0.035 radians. The total cross section is implemented as a function of β and T , the kinetic energy, with the solid angle integrated for the bracketed term in advance and evaluated numerically as a function of β^2 over the range of θ from 0.035 radians to π . Scatter at angles smaller than 0.035 radians is ignored. Results of the electron interactions as a function of the electron energy are shown in figure 2.

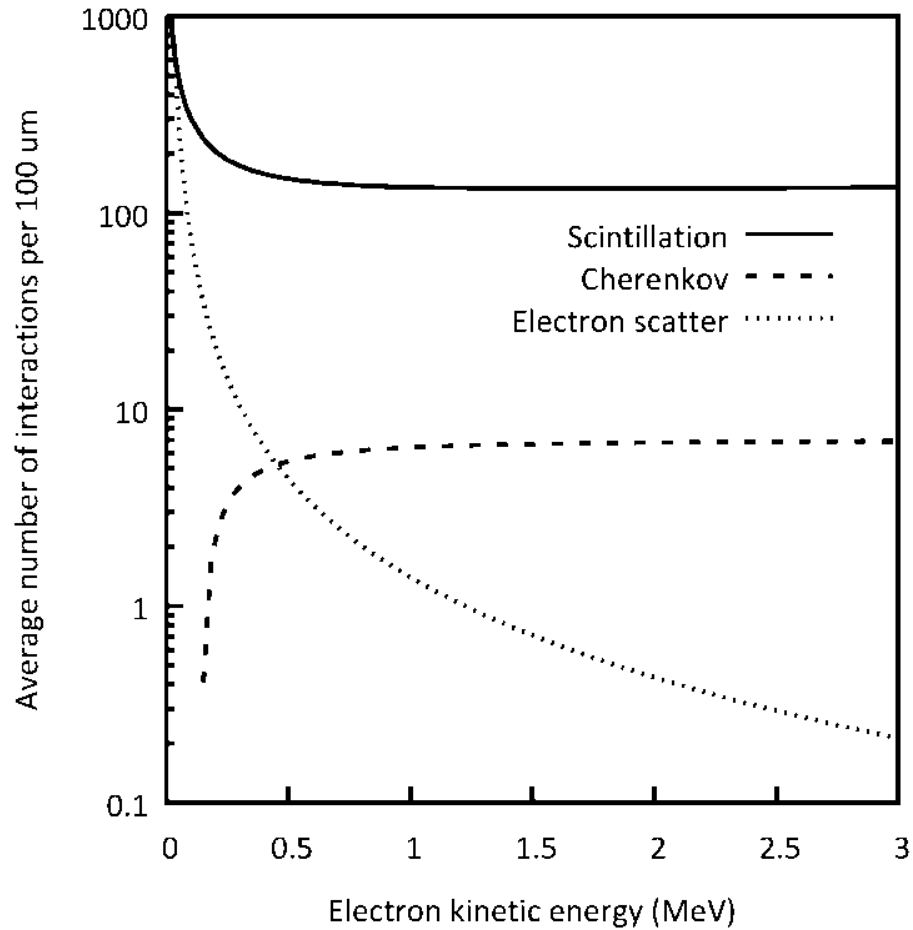


Figure 3-2. The rate of electron interactions in polystyrene fiber core material per unit pathlength as a function of the electron's kinetic energy in MeV. Scintillation is shown for an average scintillation yield of 7100 photons per MeV of deposited energy. Cherenkov photons are restricted to the wavelength range of 300 nm to 1200 nm, which is the upper spectral response of a silicon photodiode and does not account for 25% of the total Cherenkov light that would be produced above 1200 which is out of the detector range. Electron scatter accounts only for elastic scattering by soft Coulomb collisions.

The model uses the Frank-Tamm formula for determining the Cherenkov photon generation probability,¹⁷ integrated over the wavelength range of interest. Permeability μ and index of refraction n are assumed to vary negligibly over the corresponding range of angular frequencies and are treated as constants during the integration. In this approximation, we have

$$\frac{dN}{dr} = 2\pi\alpha \left(\frac{1}{\lambda_1} - \frac{1}{\lambda_2} \right) \left(1 - \frac{1}{n^2\beta^2} \right) \quad 5$$

where the number of Cherenkov photons emitted in the considered wavelength range per unit pathlength of electron travel is dN/dr , and α is the fine structure constant. We have assumed negligible electron energy loss over the path length because optical photons have energy on the order of a few eV.

The sampling method for Cherenkov radiation wavelengths uses an inverse-transform of the Frank-Tamm formula over our wavelength range as follows

$$\lambda = \frac{\lambda_{\min}}{1 - \xi \left(1 - \frac{\lambda_{\min}}{\lambda_{\max}} \right)}, \quad 6$$

and depends only on the minimum and maximum wavelength of our chosen range. The Cherenkov wavelength spectrum for various values of β is shown in Figure 3.

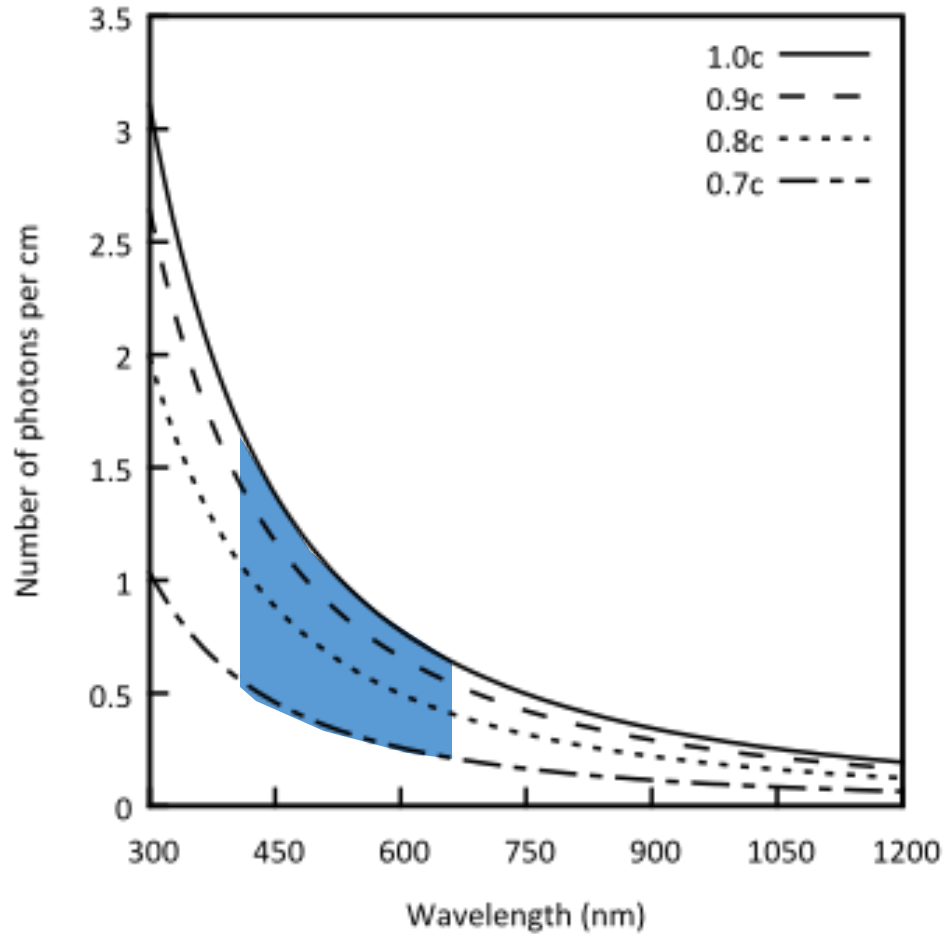


Figure 3-3. Cherenkov radiation spectrum over the wavelength range of interest in the model, 300 nm to 1200 nm. The spectrum is shown for electron velocities from 0.7c, just above the threshold for Cherenkov radiation production, in 0.1c increments up through 1.0c, the theoretical maximum electron velocity, although for clinical 6MV beams, the maximum is 0.997c and the minimum energy to produce Cherenkov radiation occurs at 0.15 MeV. The shaded region of the figure overlaps the scintillation light produced with clinical beams.

Cherenkov radiation is emitted at a specific polar angle, θ_p , relative to the velocity vector of the electron (Figure 4). We assume the azimuthal angle, ϕ_p ,

is uniformly distributed from zero to 2π in the plane perpendicular to the velocity vector. Since these angles are relative to the unit propagation vector of the electron,

$$\mathbf{\Omega}_e = l_e \hat{\mathbf{e}}_x + m_e \hat{\mathbf{e}}_y + n_e \hat{\mathbf{e}}_z, \quad 7$$

where the values of l , m , and n are the vector cosines to the respective coordinate axis, the unit propagation vector for the emitted photons in the same coordinate system is

$$\mathbf{\Omega}_p = l_p \hat{\mathbf{e}}_x + m_p \hat{\mathbf{e}}_y + n_p \hat{\mathbf{e}}_z, \quad 8$$

and the cosine factors are calculated using the following set of equations:

$$\begin{aligned} l_p &= l_e \cos\theta_p + \frac{\sin\theta_p}{\sqrt{1-n_e^2}} \times (l_e n_e \cos\phi_p - m_e \sin\phi_p) \\ m_p &= m_e \cos\theta_p + \frac{\sin\theta_p}{\sqrt{1-n_e^2}} \times (m_e n_e \cos\phi_p - l_e \sin\phi_p) \\ n_p &= n_e \cos\theta_p + \sqrt{1-n_e^2} \times \sin\theta_p \times \cos\phi_p. \end{aligned} \quad 9$$

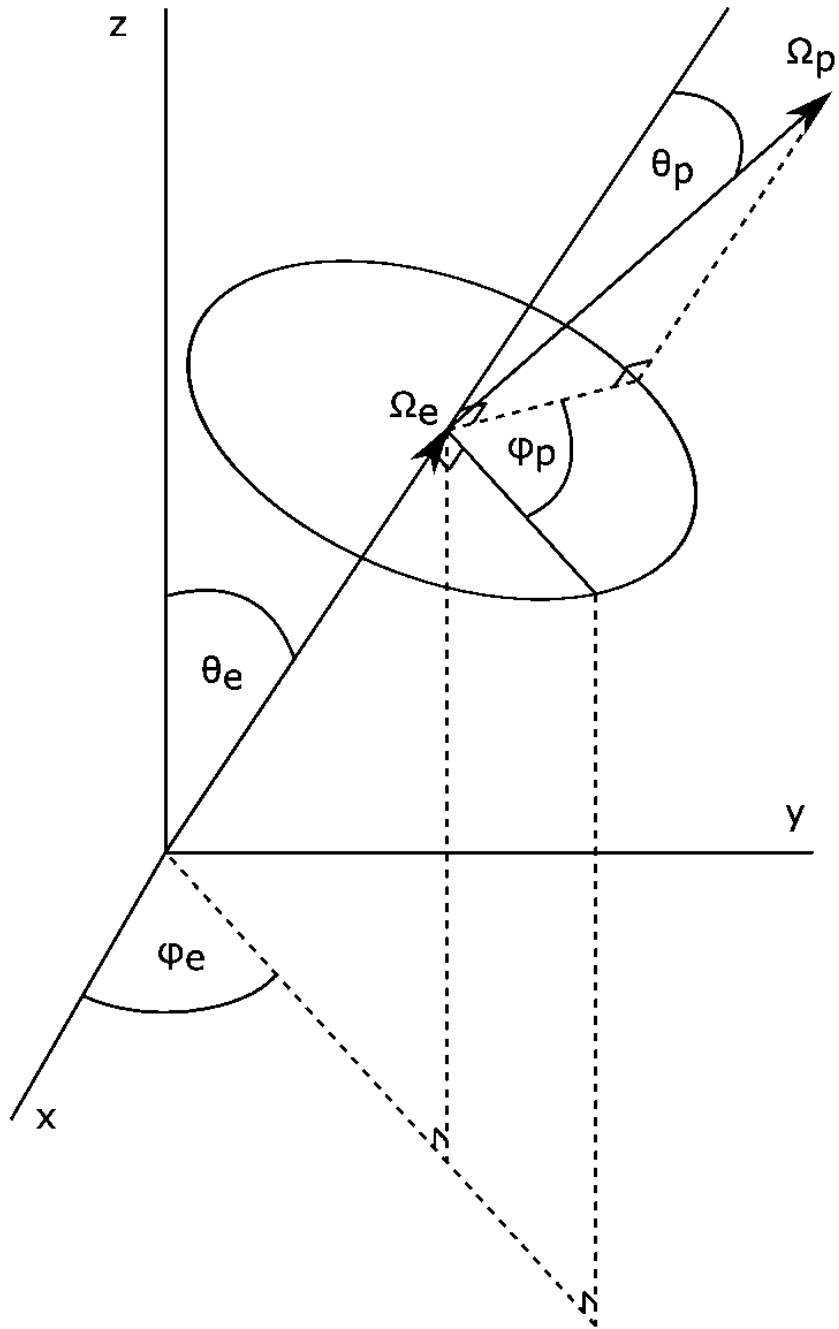


Figure 3-4. The emission angles of Cherenkov photons are distributed in a cone with its axis along the propagation vector Ω_e . Ω_p is the photon vector and θ_p is the cone emission angle

Capture of an optical photon occurs when the photon undergoes total internal reflection at the fiber core-cladding interface. Light inside the scintillating fiber travels in a straight path through the core material until it reaches the surface of the core. The cladding, which surrounds the core, has a lower index of refraction, which allows the incident light to undergo total internal reflection for angles larger than the critical angle. The incident angle at the inner surface of a square fiber can be determined from the dot product of the normal unit vector \mathbf{n}_s of the surface and the outgoing photon unit vector. The internally reflected photon propagation vector is calculated from the incident photon unit vector as follows,

$$\mathbf{\Omega}_{\mathbf{p},\text{out}} = \mathbf{\Omega}_{\mathbf{p},\text{in}} - 2 (\mathbf{\Omega}_{\mathbf{p},\text{in}} \cdot \hat{\mathbf{n}}_s) \hat{\mathbf{n}}_s . \quad 10$$

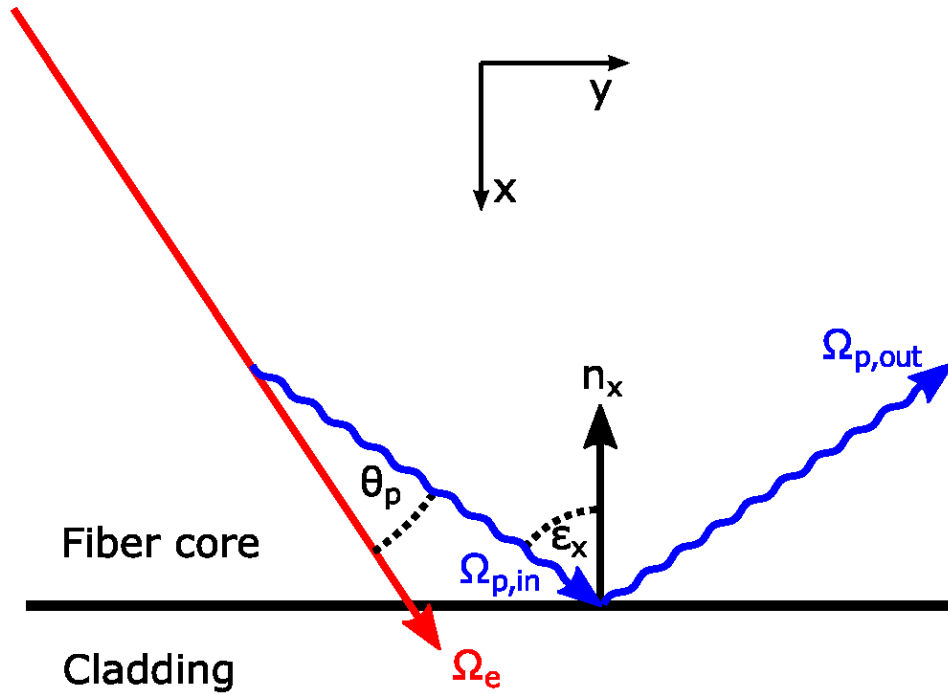


Figure 3-5: The reflection angles of Cherenkov photons at the fiber boundary are determined by the surface normal (surface perpendicular to x-axis shown here) and remain constant for a given photon.

Since the dot product of two unit vectors is the cosine of the angle between them, the incident angle at the fiber wall in the x-dimension, ε_x , and z-dimension, ε_z , is the inverse cosine of the photon propagation vector's x and z component's absolute value, respectively, with a similar result for the incident angle for round fibers, ε_r ,

$$\varepsilon_x = \cos^{-1} |l_p|$$

$$\varepsilon_y = \cos^{-1} |n_p| \tag{11}$$

$$\varepsilon_r = \cos^{-1} \sqrt{l_p^2 + n_p^2 - \left(\frac{z l_p - x n_p}{R} \right)^2} .$$

Incident and reflection angles are identical to the initial angle of incidence and reflection in both square and round fibers. If both the ε_x and ε_z for square fibers or ε_r for round fibers are greater than the critical total internal reflection angle, the Cherenkov photon will propagate in the core through a series of total internal reflections until reaching the photo-detector. Our model calculates the first incident angles and then assigns the photon as either captured or escaping, and no explicit optical photon propagation algorithm is needed.

From the initial propagation vector, we also account for photon attenuation of captured photons using implicit absorption weighting along the fiber. The photon's pathlength and the wavelength-specific attenuation coefficient determine the probability of transmitting the photon to the detector without absorption in the fiber core, and that probability is then assigned as that photon's transmitted statistical weight contribution to the total intensity in the output files. The statistic weights of the transmitted photons are further modified by the wavelength-dependent photodetector efficiency.

III. Technical characteristics of simulated fibers and detectors

The modeled fibers are Saint-Gobain formulations BCF-60 and BCF-12. The primary difference between these formulations is the scintillation yield, 7100 and 8000 scintillation photons per deposited MeV respectively, and

wavelength emission spectra which are shown in Figure 3-6 and peak at 530 nm and 435 nm respectively. Both types of fibers have a polystyrene core with an average index of refraction of 1.60, and the cladding material is acrylic with $n = 1.49$. The polystyrene core has a density of 1.06 g/cm and its atomic density composition for hydrogen and carbon is $\rho_H = 4.82 \times 10^{22} \text{ cm}^{-3}$, $\rho_C = 4.85 \times 10^{22} \text{ cm}^{-3}$, and electron density $\rho_e = 3.4 \times 10^{23} \text{ cm}^{-3}$. The manufacturer specified 1/e length, which is the length required to attenuate the overall intensity of the emission spectrum to 1/e of the initial value, is 3.5 m and 2.7 m respectively for the BCF-60 and BCF-12 fiber formulations.

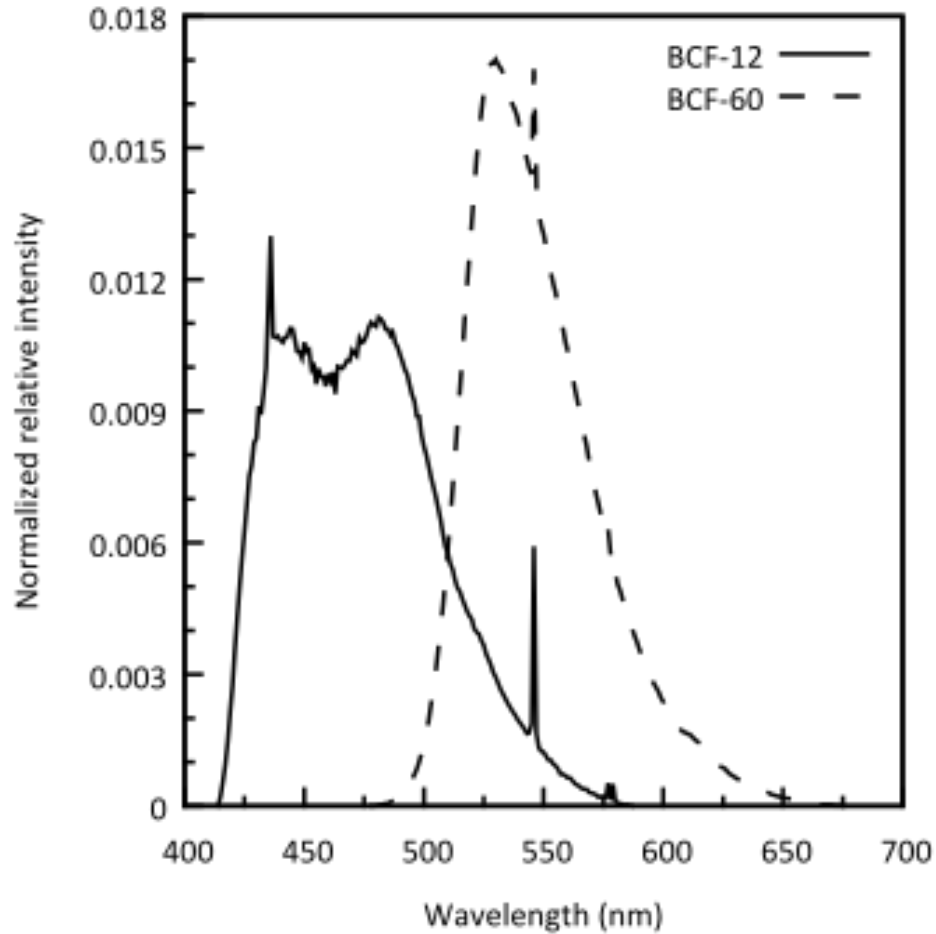


Figure 3-6. Normalized emission spectra for the BCF-12 and BCF-60 scintillator fibers. BCF-12 has a broad spectrum that peaks at 435 nm in the blue region of the visible spectrum and BCF-60 has a narrow emission in the green region of the visible spectrum with a maximum at 530 nm.

We have modeled the optical transmission properties of polystyrene (Figure 3-7) based on semi-empirical models and descriptions of photon transmission through polystyrene-core polymer optical fibers.^{18, 19} We use a wavelength-dependent equation based on a combination of the UV absorption tail, a Rayleigh scattering curve, and specific IR absorption peaks modeled

with Lorentzian distributions. In addition to the material absorption, we account for photon losses for each reflection at the fiber-cladding boundary by calculating the expected number of reflections a photon will undergo and implicitly absorbing 0.1% of that photon's weight for every reflection. This small power loss adjustment is dependent on the manufacturing process, representing losses due to imperfections in the fiber cladding,²⁰ and is therefore based on trial and error to arrive at the correct $1/e$ length as specified by the manufacturer for both scintillation distributions we modeled.

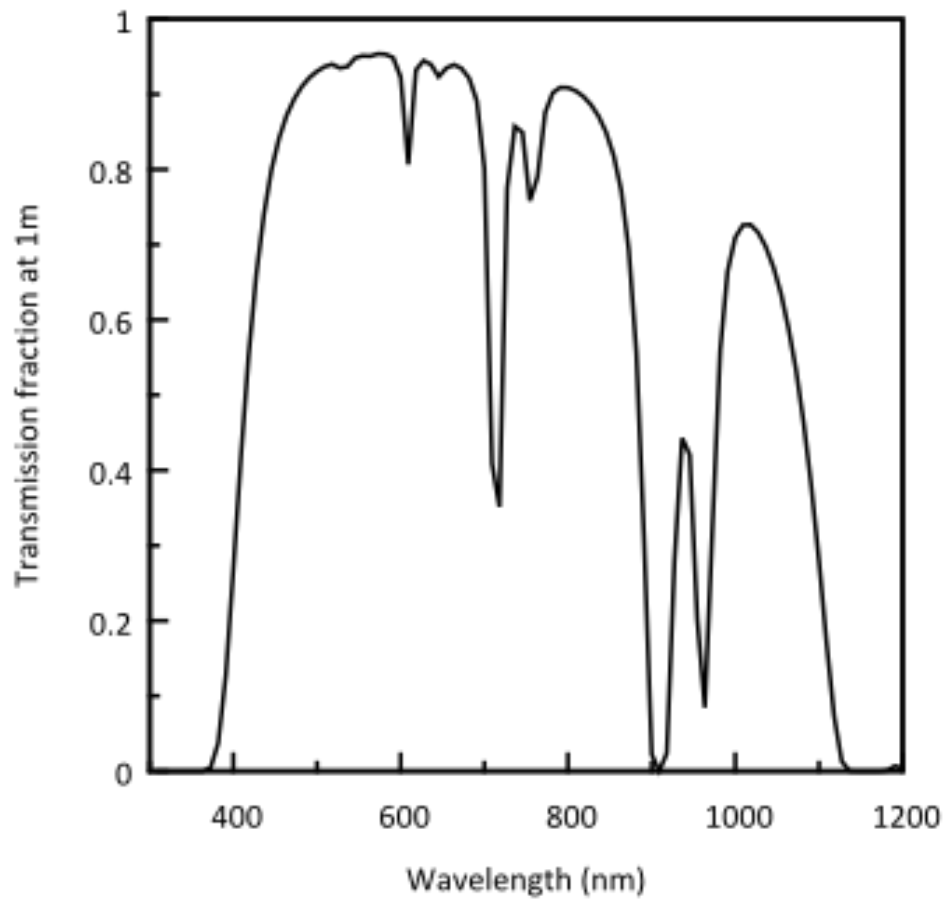


Figure 3-7. Transmission distribution used in the simulation based on a semi-empirical model of the bulk material properties of polystyrene. The plot shows the transmitted fraction of an initially uniform wavelength distribution after propagating through 100 cm of polystyrene material.

The photon detection efficiency from device specifications was interpolated in the model, and Figure 3-8 shows the photon detection efficiency as a function of wavelength for the photodiode and the SiPM. For the SiPM the photo-detection efficiency was specified from 350 nm to 640 nm in 10 nm increments with linear interpolation and was linearly extrapolated to zero at

either end. The photodiode was specified over the entire response range in 50 nm increments and interpolated with cubic splines with linear extrapolation to zero.

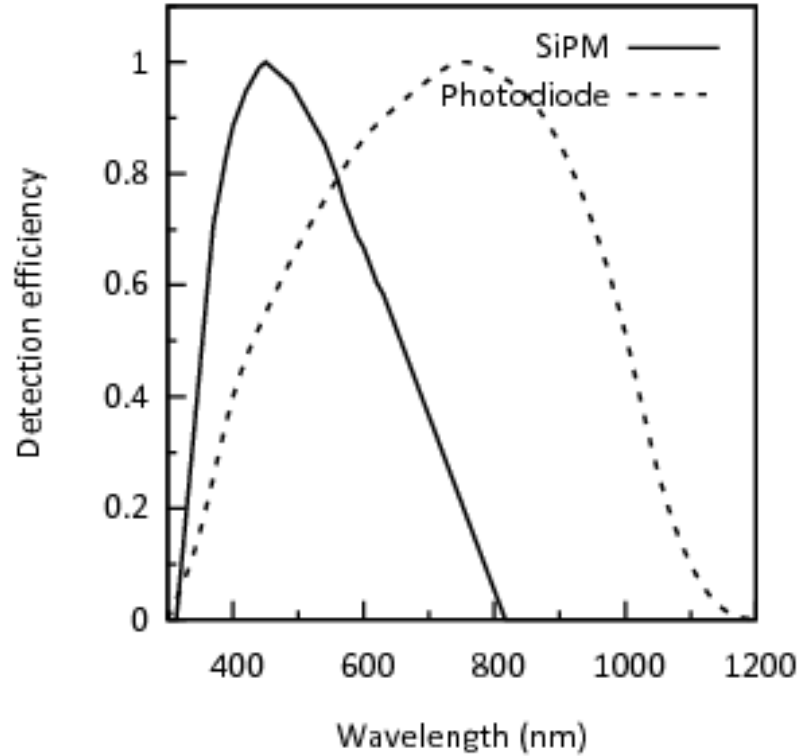


Figure 3-8. Modeled photodetectors. The photodiode was modeled with cubic spline interpolation of the data points, and it has a wide spectral sensitivity range with a 0.62 A/W peak spectral sensitivity at 850 nm. The SiPM was modeled with linear interpolation, and it has a narrow sensitivity range with a 0.48 peak detection efficiency at 450 nm. The curves are normalized to their peak value. Signal output for a photodiode is typically 1-10, while the silicon photomultiplier output increases with gain on the order of 10^6 .

IV. Results

We performed simulations using the combination of parameters shown in Table I. For each fiber set up, labeled as simulation types, we varied a parameter or combination of parameters over a set of several simulations as follows. First, in simulations of type 1, we tested the angular dependence of the fiber shapes by varying the gantry angle in 5 degree intervals for square fibers and then repeated with round fibers, and we also selected the beam modality from between 6 MeV electrons and 6 MV x-rays. In simulations of type 2 we simulated different components of the detector so that each fiber type was paired with each detector type, resulting in four combinations. In simulations of type 3 we studied the energy dependence of Cherenkov radiation by varying the initial beam energy from 1 MeV up through 20 MeV. We varied the fiber width from 0.25 mm to 2 mm in the simulations of type 4.

Table 3-I. Simulation model parameters.

Parameter	Sim type 1	Sim type 2	Sim type 3	Sim type 4
Beam energy	6 MeV electrons & 6 MV photons	6 MV photons	1-20 MeV electrons	6 MV photons
Source to fiber distance	100 cm	100 cm	100 cm	100 cm
Irradiated fiber length	10 mm	10 mm	10 mm	10 mm
Detector type	Diode	Diode & SiPM	Diode	Diode
Fiber type	BCF-60	BCF-60 & BCF-12	BCF-60	BCF-60
Fiber shape	square & round	square	square & round	square & round
Fiber width	1 mm	1 mm	1 mm	0.25- 2.00 mm
Gantry angle	-85 to 85 degrees	0 degrees	0 degrees	0 degrees

IV.A. Simulation type 1: fiber shape variation

For the first set of simulations, we investigated the role of the impinging beam angle. The fiber axis passed perpendicularly through the plane defined by the gantry axis of rotation and the vertical beam central axis. The fiber length extended 22.5 cm from the isocenter to the photodiode detector in the direction of 90 degrees gantry angle. We varied two angle-sensitive parameters: fiber shape with round and square cross-sections, and the beam varied between 6 MV x-rays and 6 MeV electrons. For the four combinations of those parameters, we investigated the range of gantry angles from -85

degrees to 85 degrees in 5 degree intervals and plotted in Figure 9 the percent of Cherenkov radiation in the total light detected at each angle.

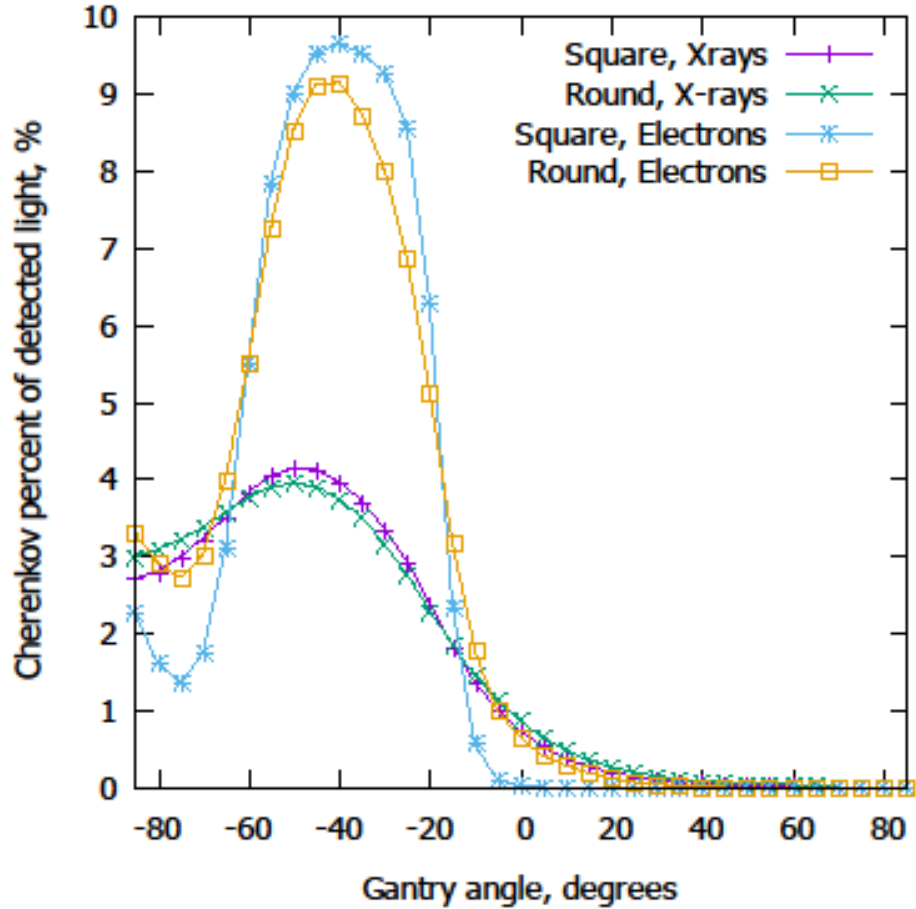


Figure 3-9. The percent of Cherenkov photons in the detected light in a square fiber and round fiber at different gantry angles for 6 MeV electrons and 6 MV photons. The detecting photodiode is at 22.5 cm from the isocenter in the direction of the gantry position at 90 degrees, and the fiber passes through the isocenter.

To verify the simulation results for x-rays, we measured the Cherenkov radiation generated inside an un-doped optical fiber coupled to a PMT

(Hamamatsu R6358P), irradiated using 6MV x-rays from an Elekta Versa linear accelerator. The measured output in Figure 10 agrees with our simulation results over the angles of greatest Cherenkov generation.

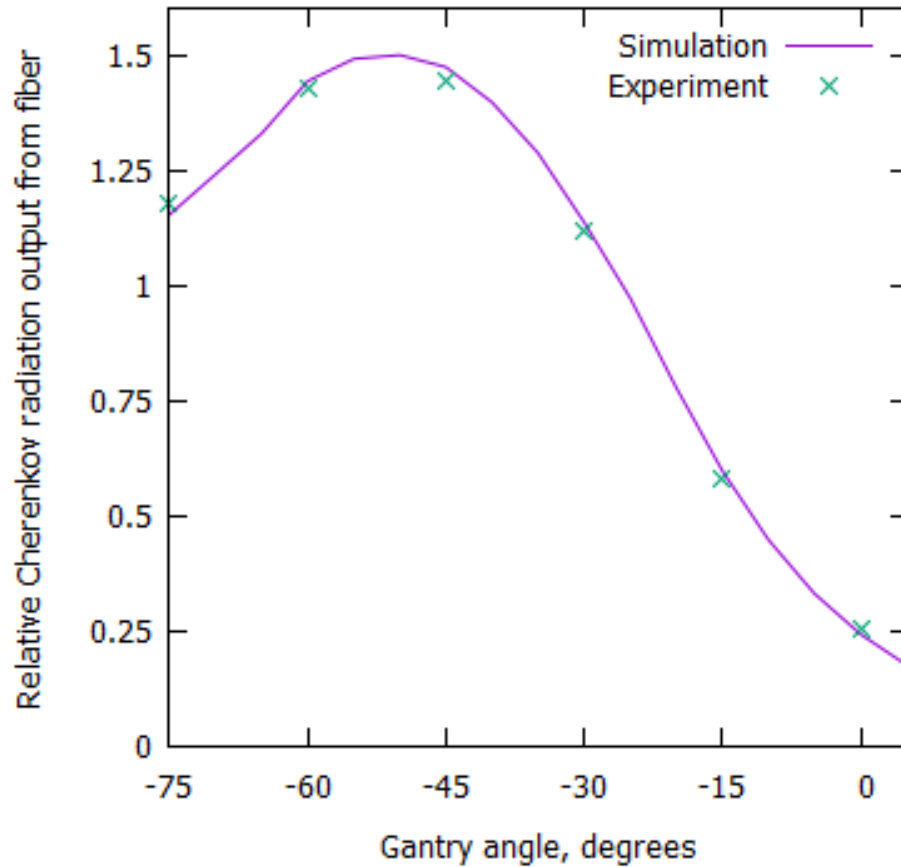


Figure 3-10. Experimental measurements of light output from an un-doped optical fiber irradiated by 6MV x-rays and coupled to a PMT follow the predicted curve from simulations.

IV.B. Simulation type 2: scintillation spectra and photodetectors

In the type 2 set of simulations, each scintillation fiber spectrum type was paired with each photon detector type for a total of four combinations. The

simulation set up was the same as type 1 simulations, but we selected only 6 MV photon beams and a fixed gantry angle at 0 degrees. We tabulated the number of photons per MeV for each combination along with the percentage of Cherenkov radiation. This output was the sum of photons detected at each end of the fiber, and the center of the fiber was coincident with the isocenter.

Table 3-II. Photon detection numbers show the signal per MeV and Cherenkov photon contribution to the total signal for each of the pairings of BCF-60 and BCF-12 with the two photodetectors.

Photon detector	Fiber type	Total photons per MeV	Scintillation photons per MeV	% Cherenkov photons of the total photons
Diode	BCF-60	423.3	420.2	0.74%
Diode	BCF-12	371.0	367.9	0.84%
SiPM	BCF-60	226.0	224.7	0.60%
SiPM	BCF-12	288.1	289.5	0.47%

Additionally, we computed the Cherenkov spectrum detected in the simulation for each detector type (Figure 3-11). The Cherenkov spectrum was sharply limited by the range of the SiPM, which accounts for the short wavelength Cherenkov photon detection of that detector. Absorption peaks at long wavelengths, arising from attenuation in the fiber core material, appear in the Cherenkov spectrum detected by the diode.

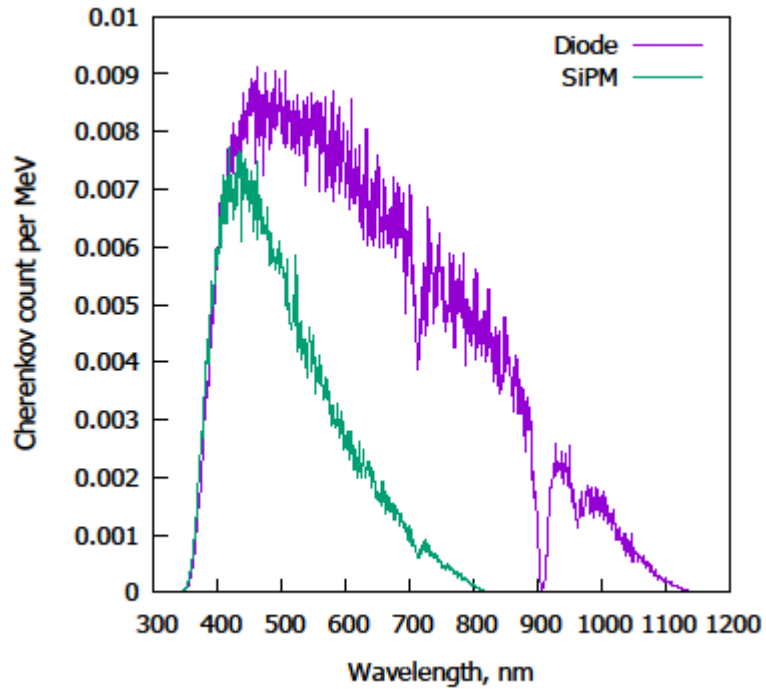


Figure 3-11. The spectrum of Cherenkov photons detected by the photodiode and the SiPM.

Scintillation light is emitted over a smaller wavelength range than the sensitive range of the photodetectors (comparing Figure 6 and Figure 8). In Table III, we calculate, based on the results in Figure 11 and the known scintillation spectrum ranges in Figure 6, the percentage of Cherenkov photons with shorter or longer wavelengths than the scintillation spectra.

Table 3-III. Cherenkov distribution relative to the scintillation emission spectra for the two detector technologies paired with each of the two fiber formulations. The percentage of Cherenkov light with shorter wavelengths than the shortest scintillation wavelength and with longer wavelengths than the longest scintillation wavelength depends on the detector sensitive range and the scintillation distribution range.

Detector	Fiber	Shorter wavelengths	Overlapping spectrum	Longer wavelengths
SiPM	BCF-12	15.6%	65.4%	19.0%
SiPM	BCF-60	46.3%	47.9%	5.8%
Diode	BCF-12	5.9%	39.9%	54.2%
Diode	BCF-60	20.7%	42.7%	36.6%

IV.C. Simulation type 3: incident beam energy

In the third set of simulations, we varied the initial particle energy from 1 MeV up to 20 MeV for a normally incident beam of electrons. The resulting curve is plotted in Figure 12. A sharp slope near the Cherenkov production threshold at low energy rose to the maximum detected fraction of around 1.4% in square fiber at 1.25 MeV and 1.6% in round fiber at 1.5 MeV. As energy increased beyond 1.5 MeV, the Cherenkov component decreased. Our simulation results revealed that the fiber cladding capture fraction of Cherenkov light approached the knee of its asymptotic value by approximately 3 MeV.

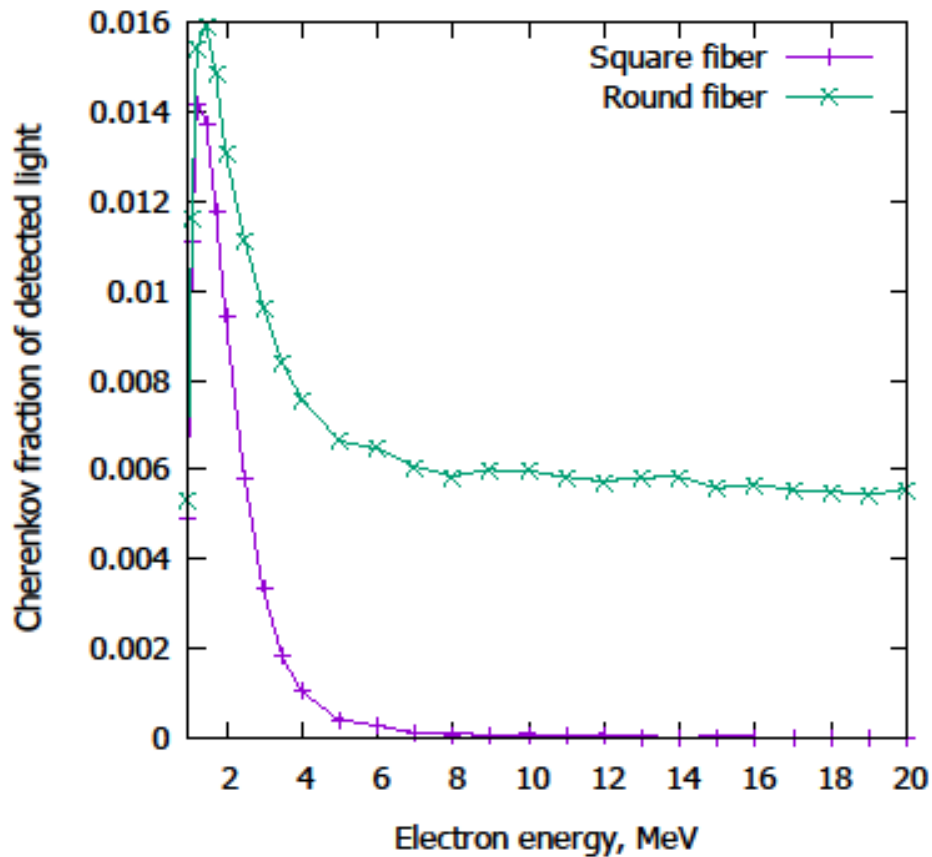


Figure 3-12. The fraction of Cherenkov photons in the detected light for electrons with incident energy of 1 to 20 MeV.

IV.D. Simulation type 4: fiber width variation

Type 4 simulations evaluated variations in fiber width, defined as the diameter of round fibers and edge-length of square fibers, and 6 MV x-rays were normally incident on the fiber, with output measured in detected photons per absorbed MeV inside the fiber core. The output curves of square and round fibers were normalized to equality at 1 mm fiber width.

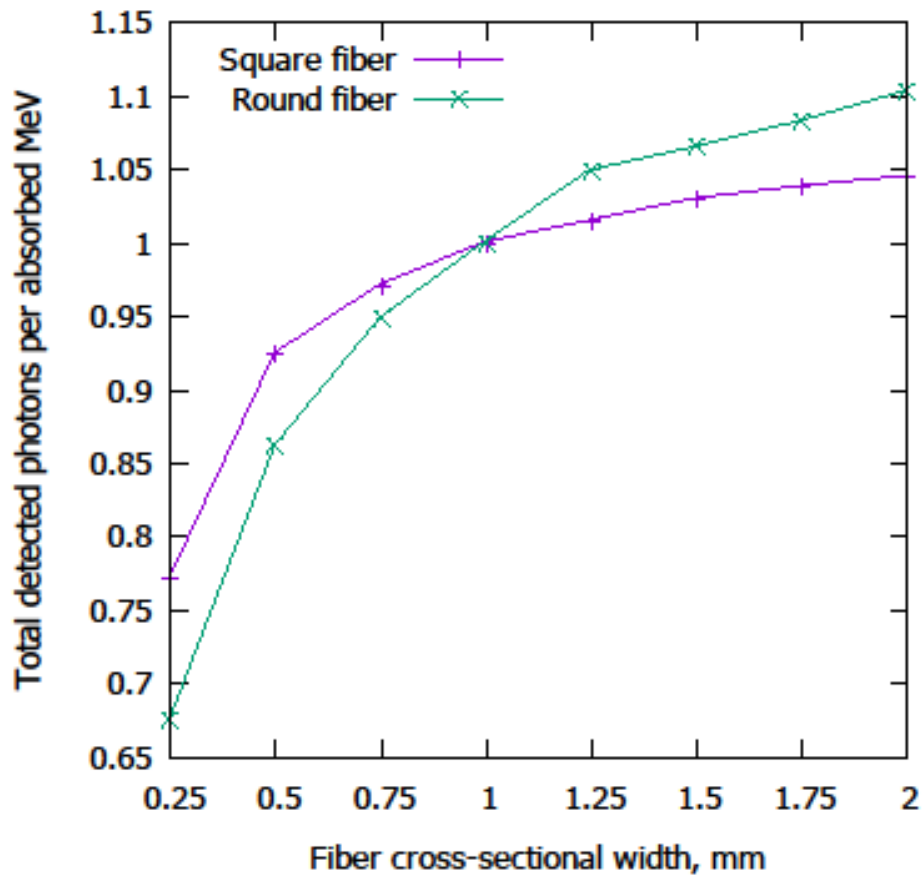


Figure 3-13. The number of photons detected per absorbed MeV decreases with decreased width of the fiber, where the width is diameter for round fibers and edge length for square fibers.

V. Discussion

V.A. Theoretical validation

Using tables of the continuous slowing down approximation (CSDA) ranges of electrons to calculate absorbed dose in a thick foil²¹, we estimate the energy deposited in the simplest case of a square shaped scintillating

fiber from a perpendicular electron beam. First, we identify the energy of the electrons entering the polystyrene core of the fiber after passing through the 0.25 cm (0.30345 g/cm²) plate of PMMA above the fiber which is the typical material thickness used in line transmission detectors. The CSDA range of 6 MeV electrons in PMMA is 3.162 g/cm². Assuming 2% path lengthening due to scattering, the energy per electron entering the PS core will average 5.415 MeV, which has a CSDA range in polystyrene of 2.85255 g/cm². The 0.10 cm (0.106 g/cm²) deep polystyrene fiber, assuming 1% path lengthening due to scatter, reduces the remaining range to 2.74549 g/cm² upon exiting the fiber, which corresponds to an average energy of 5.211 MeV per electron. The remaining energy will be deposited along the path through the lower PMMA plate before exiting into air. The energy difference between entrance and exit energy per electron, corrected for radiative losses, is an average of 0.197 MeV locally deposited in the polystyrene fiber core per electron.

Averaging repeated simulations of a 6 MeV electron beam at normal incidence on the fiber produced an average of 0.197 MeV +/- 0.001 MeV deposited in the fiber per electron. The electron processes in our simulation agrees with theory for this restricted test case.

V.B. Analysis of the main results and impact on the design and use of scintillator dosimeters in medical linear accelerators

In the design of an efficient scintillating fiber detector, we are particularly interested in the amount of Cherenkov radiation being detected with the

scintillation signal. We use as a comparison metric the fractional Cherenkov component, the amount of Cherenkov light detected divided by the total light detected. We observed variation in the Cherenkov component with variation of impinging beam angle, the beam energy, and different pairings of photodetector technologies and scintillation formulation.

The impinging beam angle had the greatest Cherenkov component when the beam pointed toward the detector end of the fiber, because Cherenkov radiation is emitted in a forward-directed cone in the direction of the detector. Electron beams peak at 9.6% Cherenkov component at 40 degrees in square fibers and 9.1% Cherenkov component in round fibers. X-ray beams are muted in comparison; the peak Cherenkov component of square fibers is 4.1% and of round fibers is 3.9%. In all combinations of fiber shape and type of beam, the Cherenkov component is less than 0.9% when the beam pointed toward the non-detecting end of the fiber, and the electron beam irradiating a square fiber in particular had a Cherenkov component of less than 0.1%.

For clinically relevant field sizes with the detector at a fixed position relative to the beam, the incident beam would have an impingement angle from approximately -10 degrees to +10 degrees. The Cherenkov component of x-ray beams would be approximately 0.4% to 1.4% in that range for square fibers and 0.5% to 1.5% for round fibers.

We found that the diode photodetector technology was more sensitive to light in general than the SiPM detector, but the diode does have a larger

Cherenkov component than the SiPM regardless of the scintillator spectrum it is paired with. Of the two scintillator spectra, we found the green-peaked BCF-60 had a higher detected light output than the blue-peaked BCF-12 scintillating fiber, regardless of detector pairing. Pairing the BCF-60 and diode photodetector produces the best output, and after analyzing the spectral distribution of Cherenkov radiation, we found only 43% of the detected Cherenkov light was inside the wavelength range of BCF-60. The idea of a band-pass filter that removes light outside of the wavelength range of the scintillator is appealing because it would eliminate over half of the detected Cherenkov light in that combination.

The Cherenkov component was sensitive to incident beam initial energy at low energies but became relatively constant for high energy beams because the Cherenkov emission angle approaches its asymptotic value beyond 3 MeV. The peak value for a normally incident beam of electrons in a square fiber was 1.4% at an electron energy of 1.25 MeV and for a round fiber was 1.6% at 1.5 MeV. For clinically realistic beams of at least 6 MeV, at normal incidence, the Cherenkov component was less than 0.1% in square fibers and on average 0.6% in round fibers.

The fiber width parameter had no measured effect on the Cherenkov component. Decreasing fiber widths decreased scintillation light transmission and Cherenkov transmission equally. The quantity of interest we found with fiber transmission was transmission losses, which was more sensitive for

round fiber diameter than square fiber. In particular, decreasing the fiber width from 1 mm to 0.5 mm caused a decrease in light output per absorbed MeV of 14% in the round fiber compared to only 8% in the square fiber.

VI. Conclusions

We are able to compute Cherenkov generation in real time scintillating fiber dosimeter geometries. The computations incorporate the major design parameters of the scintillating fiber dosimeter system, including the fiber dimensions, shapes, and emission spectra and the detector spectral response to the transported light. Variations on these parameters allow the design and optimization of high efficiency dosimeters that are capable of operating in real time to enhance patient safety and treatment accuracy of external beam radiotherapy. A variety of beam energies and beam angles enable the analysis of the dosimeter signal for various setups using either electron beams or photon beams, providing a range of results for each variation of the parameters used in the design of the scintillating fiber dosimeter.

VII. References

- ¹ A.S. Beddar, T.R. Mackie, F.H. Attix, "Water-equivalent plastic scintillation detectors for high-energy beam dosimetry: II. Properties and measurements," *Physics in medicine and biology* **37**, 1901-1913 (1992).
- ² A.S. Beddar, T.R. Mackie, F.H. Attix, "Water-equivalent plastic scintillation detectors for high-energy beam dosimetry: I. Physical characteristics and theoretical consideration," *Physics in medicine and biology* **37**, 1883-1900 (1992).

- 3 M.A. Clift, R.A. Sutton, D.V. Webb, "Water equivalence of plastic organic scintillators in megavoltage radiotherapy bremsstrahlung beams," *Physics in medicine and biology* **45**, 1885-1895 (2000).
- 4 L. Archambault, J. Arsenault, L. Gingras, A. Sam Beddar, R. Roy, L. Beaulieu, "Plastic scintillation dosimetry: Optimal selection of scintillating fibers and scintillators," *Medical Physics* **32**, 2271 (2005).
- 5 F.d. Lacroix, L. Archambault, L. Gingras, M. Guillot, A.S. Beddar, L. Beaulieu, "Clinical prototype of a plastic water-equivalent scintillating fiber dosimeter array for QA applications," *Medical Physics* **35**, 3682 (2008).
- 6 G.I. J. M. Fontbonne, G. Ban, A. Battala, J. C. Vernhes, J. Tillier, N. Bellaize, C. Le Brun, B. Tamain, K. Mercier, and J. C. Motin, "Scintillating Fiber Dosimeter for Radiation Therapy Accelerator," *IEEE TRANSACTIONS ON NUCLEAR SCIENCE* **49**, 2223-2227 (2002).
- 7 J. Lambert, Y. Yin, D.R. McKenzie, S.H. Law, A. Ralston, N. Suchowerska, "A prototype scintillation dosimeter customized for small and dynamic megavoltage radiation fields," *Physics in medicine and biology* **55**, 1115-1126 (2010).
- 8 A.S. Beddar, K.J. Kinsella, A. Ikhlef, C.H. Sibata, "A miniature "scintillator-fiberoptic-PMT" detector system for the dosimetry of small fields in stereotactic radiosurgery," *IEEE Transactions on Nuclear Science* **48**, 924-928 (2001).
- 9 B. Lee, K.W. Jang, D.H. Cho, W.J. Yoo, H.S. Kim, S.-C. Chung, J.H. Yi, "Development of One-dimensional Fiber-Optic Radiation Sensor for Measuring Dose Distributions of High Energy Photon Beams," *Optical Review* **14**, 351-354 (2007).
- 10 G. Bartesaghi, V. Conti, D. Bolognini, S. Grigioni, V. Mascagna, M. Prest, S. Scazzi, A. Mozzanica, P. Cappelletti, M. Frigerio, S. Gelosa, A. Monti, A. Ostinelli, G. Giannini, E. Vallazza, "A scintillating fiber dosimeter for radiotherapy," *Nuclear Instruments and Methods in Physics Research Section A: Accelerators, Spectrometers, Detectors and Associated Equipment* **581**, 80-83 (2007).
- 11 S.F.d. Boer, A.S. Beddar, J.A. Rawlinson, "Optical filtering and spectral measurements of radiation-induced light in plastic

- scintillation dosimetry," *Physics in medicine and biology* **38**, 945-958 (1993).
- 12 M.A. Clift, R.A. Sutton, D.V. Webb, "Dealing with Cerenkov radiation generated in organic scintillator dosimeters by bremsstrahlung beams," *Physics in medicine and biology* **45**, 1165-1182 (2000).
- 13 T. Knewton, S. Pokhrel, S. Loyalka, E. Izaguirre, "SU-F-T-559: High-Resolution Scintillating Fiber Array for In-Vivo Real-Time SRS and SBRT Patient QA," *Medical Physics* **43**, 3591-3592 (2016).
- 14 B. Lee, K.W. Jang, D.H. Cho, W.J. Yoo, G.-R. Tack, S.-C. Chung, S. Kim, H. Cho, "Measurements and elimination of Cherenkov light in fiber-optic scintillating detector for electron beam therapy dosimetry," *Nuclear Instruments and Methods in Physics Research Section A: Accelerators, Spectrometers, Detectors and Associated Equipment* **579**, 344-348 (2007).
- 15 K.W. Jang, S. Sang Hun, D.H. Cho, Y. Wook Jae, S. Jeong Ki, C. Soon-Cheol, B. Lee, P. Byung Gi, M. Joo Hyun, H. Cho, S. Kim, "Measurements of Cerenkov radiations in a scintillating fiber-optic dosimeter using a photodiode and a charge-coupled device," 477-480 (2008).
- 16 J. Motz, H. Olsen, H. Koch, "Electron Scattering without Atomic or Nuclear Excitation," *Reviews of Modern Physics* **36**, 881-928 (1964).
- 17 K. Nakamura, "Review of Particle Physics," *Journal of Physics G: Nuclear and Particle Physics* **37**, 075021 (2010).
- 18 T. Kaino, "Low-loss polystyrene core-optical fibers," *Journal of Applied Physics* **52**, 7061 (1981).
- 19 J. Zubia, J. Arrue, "Plastic Optical Fibers: An Introduction to Their Technological Processes and Applications," *Optical Fiber Technology* **7**, 101-140 (2001).
- 20 M. Kitazawa, A.D. Bross, J.F. Kreidl, R.E. Steele, "Scintillating plastic optical fiber radiation detectors in high-energy particle physics," in *SPIE Conference on Optical Fiber Technology, Vol. 1592* (Boston, Massachusetts, 1991), pp. 122-132.
- 21 F.H. Attix, W.C. Roesch, E. Tochilin, *Radiation dosimetry*, 2d ed. (Academic Press, New York, 1966).

CHAPTER 4: A two-layer cutaneous tissue model of external beam radiotherapy induced Cherenkov emission

Purpose: Quantitative imaging of the emitted Cherenkov light is a putative method to study skin ionizing radiation effects using the optical properties of the Cherenkov light emitted from patient's skin exposed to an MV external therapy beam of x-rays or electrons. We model the angular, spectral, and surface distribution of the Cherenkov intensity to determine its relation with cutaneous melanin and hemoglobin oxygenation state.

Methods: To characterize the emitted Cherenkov light distribution, we developed a tissue model simulating the interaction of a primary MV beam with skin and the optical interactions of the emitted Cherenkov light with affected skin layers. The cutaneous model consists of a semi-infinite dermal region and an overlying thinner epidermal layer. The algorithm stresses the distinct optical absorption and scattering occurring in each tissue medium.

Results: The spectrum of Cherenkov light emitted from the irradiated skin surface shows absorption bands corresponding to hemoglobin absorption lines from the dermal layer, originating from the process of ionizing radiation penetration to the dermal region and generation of back propagated Cherenkov radiation across the dermis. The resulting spectrum of Cherenkov radiation has wavebands at 454-500nm and 586-796nm that are sensitive to biological changes in tissue oxygenation. We quantified the oxygen saturation

sensitivity ranging from 0% to 100% for Cherenkov radiation in these bands and parameterized this sensitivity for variations of the melanosome volume fraction typical of the human epidermal layer ranging from 1.3% to 45%.

Conclusions: Cherenkov emission from the irradiated skin surface depends on the concentration of oxygenated and deoxygenated hemoglobin in the dermis and the melanosome content of the epidermis, which allowed us to estimate the sensitivity of certain wavebands to oxygen saturation for detecting skin response to treatment of skin lesions such as keloids or skin cancers. Optimal waveband selection depends on the melanin content of the skin, with short wavebands providing the strongest signals from lightly pigmented skin.

I. Introduction

An emerging method of real-time dosimetry in external beam megavoltage radiation therapy is based on the Cherenkov photons emitted from the patient's skin during the treatment arising from interactions of high energy electrons and the skin tissue. It has been shown that the Cherenkov light intensity can be directly imaged with high-efficiency ICCD and EM-ICCD optical cameras to verify accurate treatment delivery while the beam is on¹. Additional to dosimetry, the relationship between Cherenkov light intensity with the incident treatment beam fluence or skin dose can provide additional information of the skin interaction to ionizing and skin biological properties.² Estimating the intensity and spectral characteristics of Cherenkov light

generated within the tissue offers great challenges. While in Cherenkov based dosimetry, intensity emission is the quantity of interest, the emission spectrum (absorption) can provide information about patients' radiation skin reactions, skin tissue composition, and oxygenation.

To determine the usefulness of Cherenkov emission for dosimetry, the theoretical relationship between radiation dose and Cherenkov radiation generation has been studied² using analytic and Monte Carlo methods for various radiation beam sizes, modalities (bremsstrahlung, Co-60, and electron beams), and energies, although the absorption and scattering of Cherenkov light was not included in previous studies. Here, to accurately account for Cherenkov emission from skin as a surrogate for skin-ionizing radiation interaction and skin composition, the Cherenkov radiation generation and its optical transport through tissue is explicitly modeled using a parametrization of the skin optical and ionizing radiation absorption and scattering properties.

II. Methods

Monte Carlo is used to simulate the ionizing radiation interactions with the medium, water or skin, as well as propagating the optical photons through the medium to the point of emission at the air-skin surface. We report the estimated distributions of Cherenkov photons that are emitted from the surface of the medium.

We focused on the cutaneous layer by restricting the model to a practical range of 30mm, which comprises the maximum back propagation distance expected from secondary electrons generated by a 6MV beam. The initial statistical weight of secondary electrons are scaled by the interaction probability across this 30mm depth, and is fully accounted for in the subsequent Cherenkov light distributions as a function of skin depth.

II.A. X-ray interactions

We consider a beam of 6MV x-rays entering the tissue at normal incidence as shown in Figure 1. The beam undergoes photoelectric interactions and Compton scattering interactions.

To minimize statistical variance in our results while sampling relatively rare photoelectric events, for an x-ray's first interaction event we split the statistical interaction weight of secondary electrons between an electron generated after a photoelectric event and an electron from a Compton scattering event, which has an energy-dependent directional distribution. The scattered Compton photons undergo further interactions to generate additional electrons until the photons are absorbed in a photoelectric event.

Photoelectric events count for less than 1% of interactions above 0.2 MeV, which is the electron energy threshold to produce Cherenkov radiation, so photoelectric interactions were accelerated in the simulation by sampling photoelectron trajectories from an isotropic distribution and ignoring binding energy. In the case of Compton scattering events, we based the Compton

electron's trajectory and energy on the well-known Klein-Nishina cross-section formula³.

We modeled both skin layers as homogeneous material with uniform radiation characteristics from the ICRP skin composition data as weight fractions: H[0.100588], C[0.228250], N[0.046420], O[0.619002], Na[0.000070], Mg[0.000060], P[0.000330], S[0.001590], Cl[0.002670], K[0.000850], Ca[0.000150], Fe[0.000010], and Zn[0.000010]. Other ICRP properties used in the model are the physical density, 1.10 g cm^{-3} , and the mean ionization energy, 72.7 eV .^{4, 5} Interaction probabilities for x-rays are based on data from the NIST XCOM Photon Cross Sections Database⁴ using the composition data.

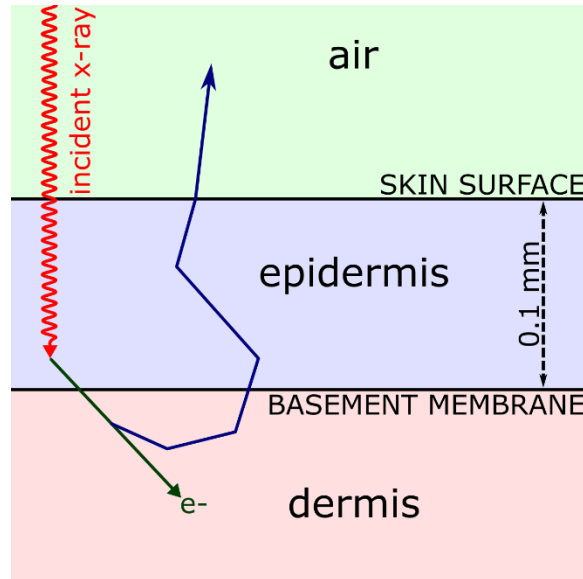


Figure 4-1. Diagram of the two-layer skin model with a 0.1 mm thick epidermal layer overlying the dermal layer.

II.B. Electron interactions

The x-rays produce secondary electrons, which then interact throughout the medium and will produce Cherenkov radiation if Cherenkov emission constraints – electron energy above 219-keV for a medium with a 1.4 refractive index – are satisfied⁶. We chose to use the typically selected refractive index of 1.47, which factors into both the Fresnel refraction equations and the Frank-Tamm formula,

$$\frac{dN}{dL} = 2\pi\alpha \left(\frac{1}{\lambda_2} - \frac{1}{\lambda_1} \right) \left(1 - \frac{1}{\beta^2 n^2} \right) \quad 12$$

with units of Cherenkov photons per unit pathlength. The constant α ,

approximately $1/137$, is the fine structure constant, the wavelength range of interest is the interval $[\lambda_1, \lambda_2]$, n is the medium's refractive index, and $\beta=v/c$ is the relative electron velocity.

The particle tracking for electrons included interactions for soft collisions, Coulomb scattering, and Cherenkov radiation production using the Frank-Tamm formula. For energy deposition by electron interactions, we interpolated the stopping power tables from the NIST ESTAR database⁵ as an approximation of the energy lost by soft collisions. For the electron scattering process, we use Coulomb scattering based on the Mott-Born approximation with no shielding and a point nucleus.⁸

II.C. Optical interactions

The Cherenkov radiation propagates through the medium, undergoing absorption, scattering, and surface reflection which are modeled using optical absorption coefficients and anisotropy factors found in the literature^{7, 9-12}. The skin was divided into two homogeneous layers: the epidermis and the underlying dermis to compute the optical photon propagation. We used a thickness of 100 microns for the epidermis, and the remaining depth for the dermis⁷. Each layer has separate optical absorption coefficients, scattering coefficients, and anisotropy factors.

We modeled the optical absorption in the epidermal layer and the dermal layer as the absorption by major molecular absorbers found in each layer using the methodology developed by Prahl⁹ and tissue values calculated from

the work by Jacques (figure 2).¹² The epidermal layer optical absorber is melanin, which varies significantly in the human population, with melanosome volume fraction ranging from 1.3% to 43%.⁷ The dermal layer absorber is hemoglobin, in the oxygenated and deoxygenated state, with a dermal molarity of 4.7 μM and typical oxygen saturation of 40%. To accelerate our model so that each sampled wavelength contributes to as much volume as possible, we use implicit absorption during transport to gradually reduce the photon statistical weight until reaching the weight-based termination threshold of 10^{-3} , at which point absorption interactions are sampled competitively against scattering interactions with photon termination occurring upon the sampling of an absorption event.

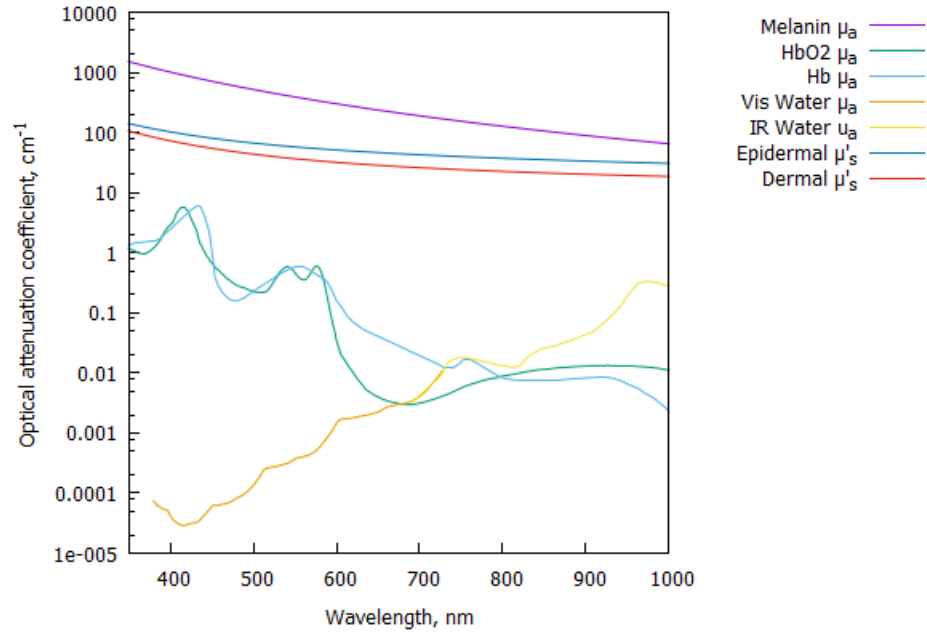


Figure 4-2. Wavelength-dependent optical interaction coefficients for human skin in the visible range and extending out to 1000nm. Epidermal absorption occurs by melanin, dermal absorption occurs by a mixture of oxygenated hemoglobin (HbO₂), deoxy-hemoglobin (Hb), and water. Reduced scattering coefficients for the epidermis and dermis are also shown.

The wavelength dependent scattering interaction probability for the dermis and the epidermis was determined using reduced scattering coefficient data from each layer independently as reported in the literature^{11, 12}. The data for the reduced scattering coefficient, which characterizes attenuation by scatter, does not describe the directional distribution of the scattered photons, so the model contained a tissue specific anisotropy factor from literature data^{7, 10} to account for the full scattering interaction during the simulation. The anisotropy factor g for dermis is a constant 0.715 across

the visible range and in the epidermis is defined by the following exponential relation $g(\lambda) = 0.745 + 0.546(1 - \exp(-(\lambda - 500.0)/1806.0))^{10}$. We sampled the scattering angles θ using those values of the anisotropy factor g and the Henyey-Greenstein phase function,

$$\cos\theta = \frac{1}{2g} \left[1 + g^2 - \left(\frac{1 - g^2}{1 - g + 2g\xi} \right)^2 \right] \quad 13$$

where ξ is a normalized uniform random number.

Photons crossing the plane of the skin-air interface undergo partial reflection, splitting the photon statistical weight into a reflected and transmitted photon, with angles determined using Snell's law, which set the fractional weight of the reflected photon from the Fresnel reflection coefficient¹³. The reflected photon propagated further throughout the tissue, while the transmitted photon carrying the remaining statistical weight contributes to the Cherenkov light intensity output estimation. We chose a photon propagation cut-off depth of 5mm by considering that fewer than 10^{-7} optical photons would survive to reach the skin surface from beyond that depth, and to implement that cut-off we use a Russian roulette method to eliminate 90% of the particles crossing that depth. The extension of the transverse plane is determined by tracking optical photons until the photon was absorbed.

II.D. Comparison to skin surface diffuse reflection

For comparison to diffuse scatter of ambient lighting, we replaced the x-ray beam with an incident beam of optical photons with uniform distribution over the visual and near infrared spectrum, from 350nm to 1000nm. We record the photons that are backscattered out of the tissue. The resulting remission can be used to determine the signature of the Cherenkov properties relative to incident visible light, which have different spectra, initial distributions, and angular distributions, to explore the sensitivity of skin propagation to those parameters.

II.E. Comparison to Cherenkov generation and emission in water

For comparison and interpretation of results we replaced tissue with water in our model. The x-rays enter the water slab at normal incidence from the air slab, and we record the number of Cherenkov photons returning to the air-water surface, which allows comparison of the signature of the skin optical scattering and absorption in the Cherenkov emission.

The radiological interactions in the water material are computed using the same algorithm as the tissue layers. Visible Cherenkov photon transport through the water medium are computed using the absorption coefficients for water¹⁴ shown in Figure 2. In tissue scattering occurs through a combination of Mie and Rayleigh scattering originating from the organized structures in cells that cause light to undergo one of these two modes of scatter¹⁵, but in pure water scattering arises from microscopic density fluctuations in the

medium caused by thermal molecular motion, which is described in the Einstein-Smoluchowski theory of scattering.¹⁶ The scattering coefficient $b(\lambda)$, equation 4, is independent of the scattering angle,

$$b(\lambda) = \frac{8\pi}{3} \frac{2+\delta}{1+\delta} \left(\frac{\lambda_0}{\lambda} \right)^{4.32} \tilde{\beta}(\pi; \lambda_0) = 1.008 \times 10^9 \lambda^{-4.32} \quad 14$$

with λ in units of nm. The angular phase function $\beta(\theta)$, equation 5,

$$\beta(\theta) = \frac{3}{8\pi} \frac{1+\delta}{2+\delta} \left(1 + \frac{1-\delta}{1+\delta} \cos^2 \theta \right) = 0.06225 (1 + 0.8349 \cos^2 \theta) \quad 15$$

is independent of the wavelength. The constant factors in each equation were evaluated based on a depolarization ratio $\delta=0.09$ and normalization to an attenuation factor of $0.94 \times 10^{-4} \text{ m}^{-1}$ at $\lambda = 546\text{nm}$ and $\theta = 180$ degrees.¹⁶

III. Results

We simulated a square $1 \times 1 \text{ mm}^2$ normally incident x-ray beamlet containing 10^6 poly-energetic 6-MV photons. For our initial simulations we set the biological parameters to 2.5% melanosome fraction by volume in the epidermis and 40% oxygen saturation (SO₂) of hemoglobin in the dermis.

III.A. Cherenkov generation at depth

Figure 3 displays the resulting Cherenkov intensity generated in tissue (3a) and water (3b). There is a Cherenkov buildup region near the surface where the electron fluence is low and a gradient at the edge of the beam where the fall off of lateral electron fluence causes loss of Cherenkov radiation. The total Cherenkov intensity shown in the figure is approximately

34% higher in tissue than in water because we set the refractive index of tissue to 1.4 and the Frank-Tamm formula relates higher indices of refraction to increased Cherenkov emission. Additionally, the refractive index dependent threshold for Cherenkov radiation allows tissue to generate Cherenkov radiation at electron energies down to 219keV compared to the threshold of 289keV in water.

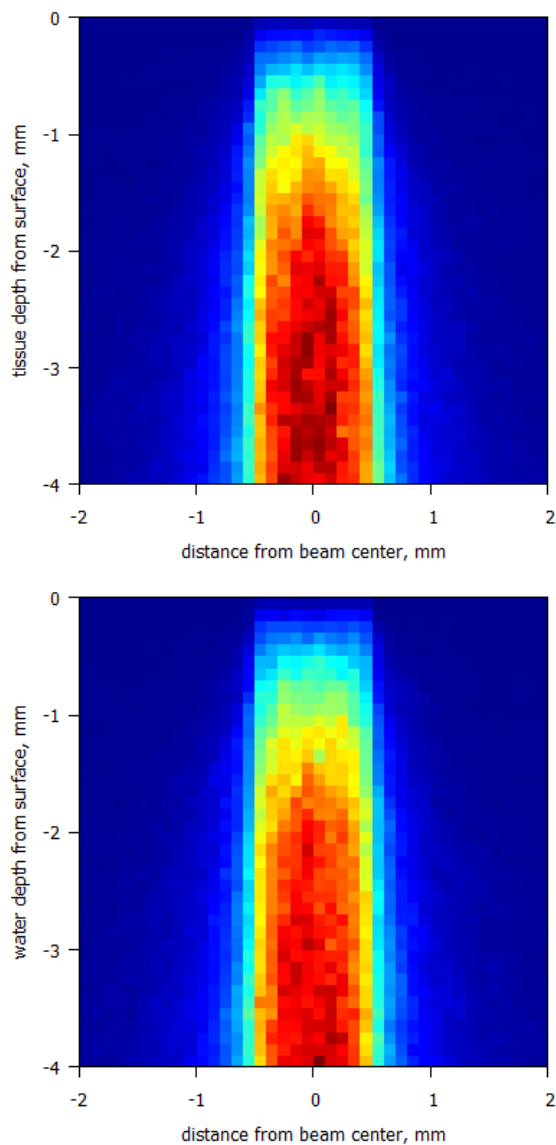


Figure 4-3. Cherenkov intensity distributions at the moment of generation in the media for radiation beamlets impinging at normal incidence into an air-medium interface. For both figures the vertical axis shows depth in tissue, with the air boundary at the top (depth=0), extending downward to a depth of 4mm, and the horizontal axis shows the transverse cross-section through the center of the 1 mm² 6-MV x-ray beamlet. The medium on the left (a) is tissue and on the right (b) is water.

III.B. Surface distributions

We evaluated the lateral extent of the surface distribution of optical Cherenkov photons emitted from the skin surface. The surface isodose lines from $0.1 \times 0.1 \times 4.0 \text{ mm}^3$ dose voxels, Figure 4a, have a steeper gradient than the emitted Cherenkov intensity contours in Figure 4b: the surface dose had a full width at half-maximum (FWHM) of 1.0 mm centered at the 1mm-wide beamlet center while the Cherenkov FWHM was 1.8 mm. Diffusely backscattered visible light in Figure 4c showed the effects of lateral optical scattering in tissue, and the FWHM was 1.0 mm.

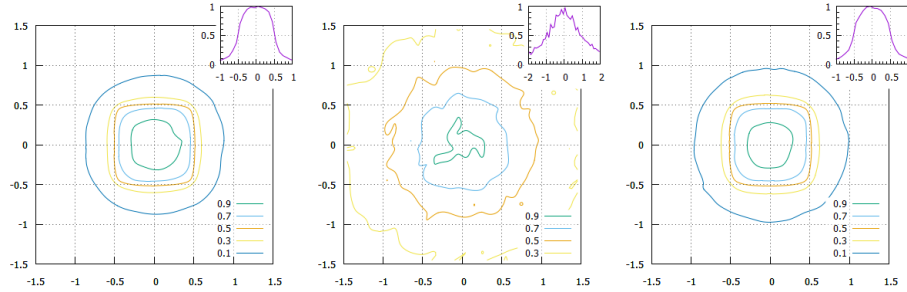


Figure 4-4. Top down views of the air-tissue surface centered at the $1 \times 1 \text{ mm}^2$ beamlet, with insets showing the horizontal profile line through the center of each corresponding plot. a) Isodose distribution contours showing the average dose in the upper 4 mm tissue layer for the 6 MV photon beam, b) the corresponding Cherenkov emission intensity from the tissue at the surface, and (c) backscattered light for a normal incidence optical beam. Normalization is to maximum intensity and the dimensions are in mm.

III.C. Angular distributions

For each case of study, the angular distribution of photons per unit solid angle, normalized to the total number of photons (figure 5), was forward scattered and had the highest intensity near the normal to the skin-air interface plane. The Cherenkov distribution in tissue was most forward scattered at 0.36 Sr^{-1} on average within the first 5 degrees from the normal. The optical beam's backscattered distribution closely followed the Cherenkov emission, peaking at 0.34 Sr^{-1} , and the Cherenkov emission from water was the least forward-peaked at 0.28 Sr^{-1} . The curve for diffuse reflection from an ideal diffuse scattering material (0.32 Sr^{-1} peak) is shown for comparison.

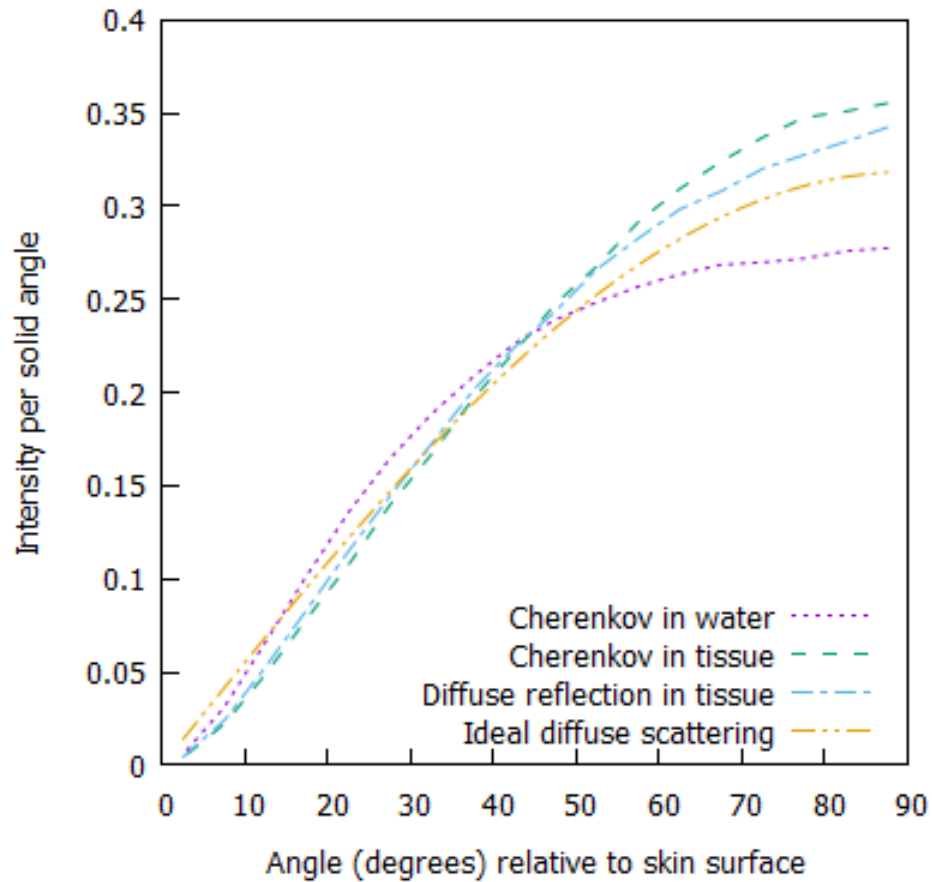


Figure 4-5. Emitted intensity plot of the directional distribution per unit solid angle (Sr^{-1}) of emitted light with 5 degree binning. The surface normal is designated as 90 degrees. Curves are each normalized to a total photon emission of unity before calculating the emission per solid angle.

III.D. Spectral distributions

Figure 6 shows a comparison of the simulated spectral distribution of the photon intensity emitted from the air-skin surface by Cherenkov light, from the air-water surface, and for diffusely scattered light from human skin. The two absorption bands shown in the spectra of the Cherenkov light emitted

from the tissue corresponds to the location of the dermal hemoglobin absorption peaks. Diffusely scattered light from the incident optical beam showed less pronounced hemoglobin absorption than the Cherenkov emission generated by the x-ray beam, and they are not present in Cherenkov radiation emitted from water.

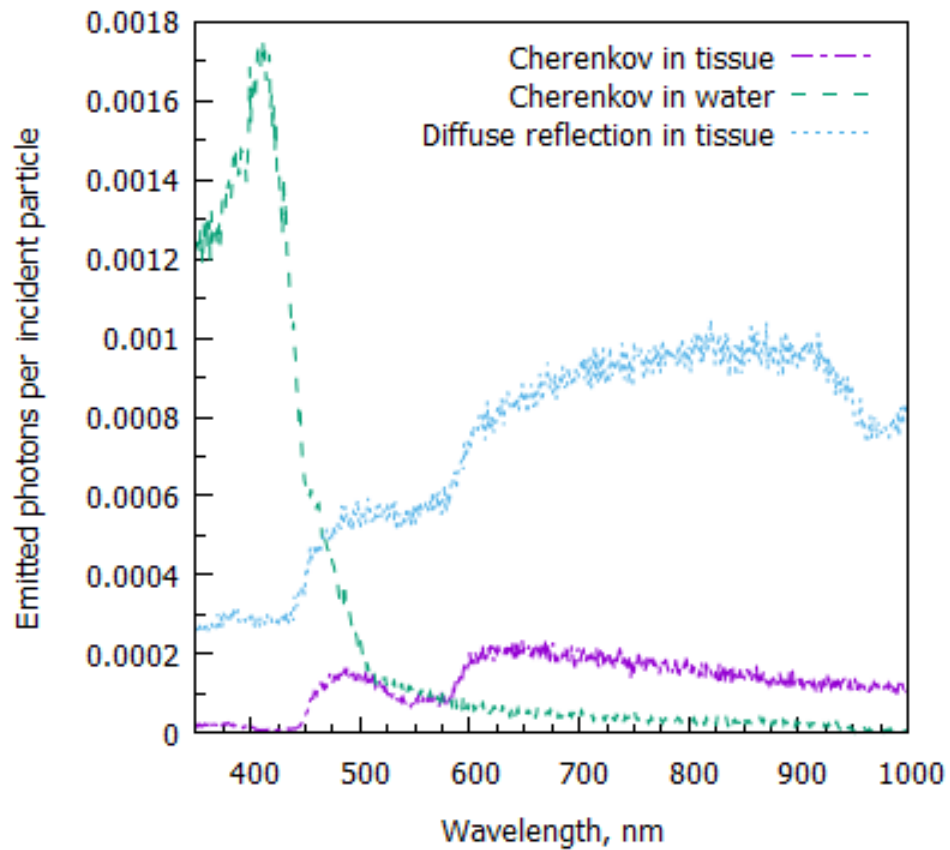


Figure 4-6. The photon spectral distribution of the emitted light ranging in wavelength from 350nm to 1000nm for Cherenkov emission from the skin, Cherenkov from water, and diffusely reflected optical light from the skin model. The vertical axis is normalized to emitted photons per incident particle (either Cherenkov photons per x-ray or diffusely reflected photons per incident photon).

III.E. Spectral sensitivity to dermal melanosome fractional volume

The biological parameters have so far been set to 40% SO₂ in the dermal hemoglobin and 2.5% melanosome volume fraction. Now we show results for

the simulation with variations in the epidermal melanosome volume fraction of 1.3%, 2.5%, and 5% to 45% in 5% increments.

The spectrum of Cherenkov radiation is generated in inverse proportion to the cube of its wavelength, but the emitted Cherenkov radiation carries the spectral signature of optical chromophores, hemoglobin and melanin, in the tissue layers it passed through (figure 7). Two high transmission spectral regions appear: one near 500nm and the other beyond 600nm. Included within the first peak is the wavelength band from 454-500nm, which permits higher transmission through deoxygenated hemoglobin than through oxygenated hemoglobin. The second peak contains the wavelength band 586-796nm, where oxygenated hemoglobin allows higher transmission than deoxygenated hemoglobin.

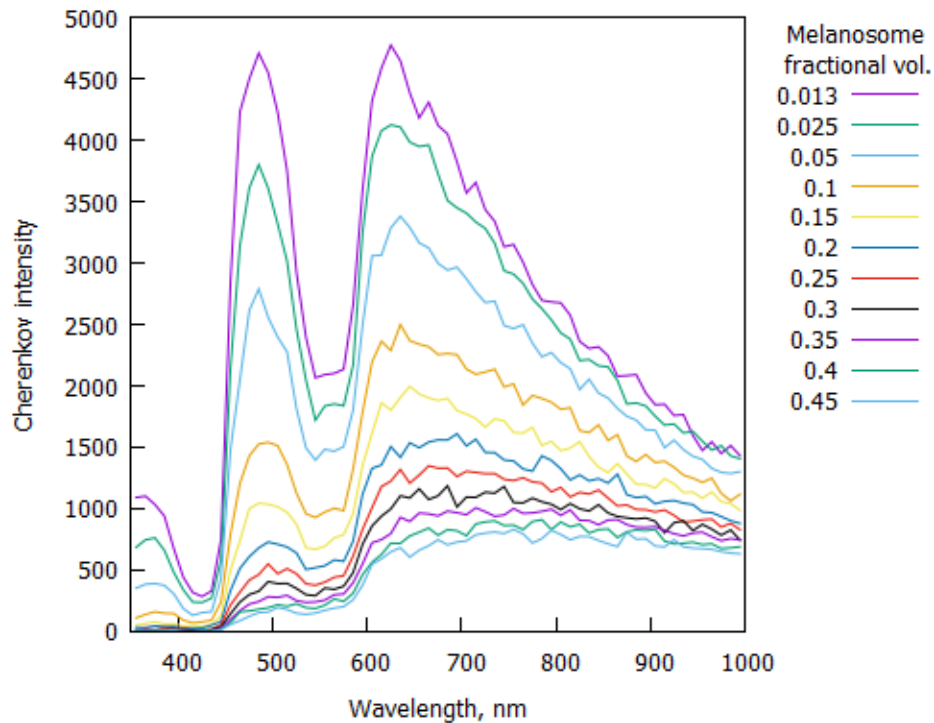


Figure 4-7. Cherenkov radiation spectrum emitted from skin with 10nm binning. Skin parameters are set to 40% oxygen saturation and a range of epidermal melanosome volume fraction from 0.013 to 0.45.

III.F. Spectral sensitivity to dermal oxygen saturation

To further investigate the two transmission bands in the previous section, we ran simulations varying the oxygenation of the dermal hemoglobin from 0% to 100% in 5% SO_2 increments. Hemoglobin oxygenation in skin can be spectroscopically measured because the absorption spectrum for hemoglobin differs for oxygenated and deoxygenated states of hemoglobin. Oxygenated hemoglobin absorbs more strongly over the wavelength band from 454-500nm, and in that wavelength band the emitted Cherenkov radiation

decreased with increased dermal oxygenation (figure 8). In the 586-796nm wavelength band, where deoxygenated hemoglobin more strongly absorbs, the detected Cherenkov radiation increased with dermal oxygenation (figure 9). The slopes of these lines indicate the sensitivity of each band to dermal hemoglobin SO₂. Generally, increasing dermal oxygenation increases Cherenkov emission in the 586-796nm band while decreasing Cherenkov emitted at 454-500nm.

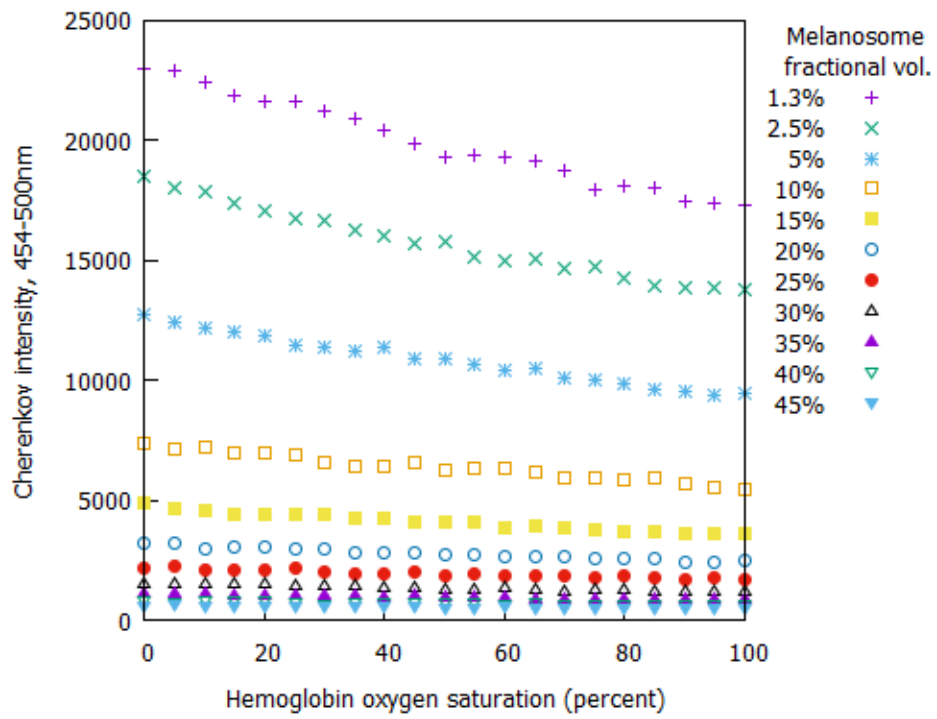


Figure 4-8. The Cherenkov intensity in the 454-500nm wavelength band as a function of oxygen saturation. The curves are parameterized to the melanosome volume fraction, ranging from 1.3% to 45%.

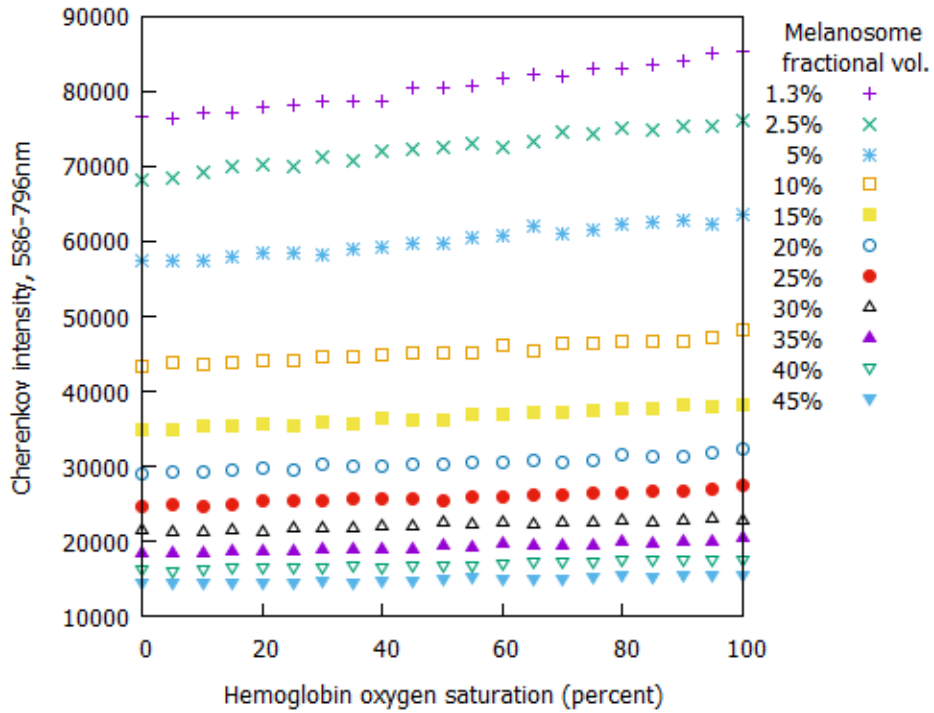


Figure 4-9. The Cherenkov intensity in the 586-796nm wavelength band a function of oxygen saturation. The curves are parameterized to the melanosome volume fraction, ranging from 1.3% to 45%.

III.G. Cherenkov intensity estimates of oxygen saturation are sensitive to melanin

The previous results show that the long wavelength band is more sensitive than the short wavelength band to changes in tissue oxygenation, but now we demonstrate that both bands are more sensitive to variations in melanin concentration than to tissue oxygenation. The data from the figures 5 and 6 are re-plotted together as a function of melanosome volume fraction ranging from 1.3% to 45% (figure 10). For increasing amounts of melanin, the

decrease in oxygenation sensitivity of the 454-500nm wavelength band was 74% less than the decrease in the 586-796nm wavelength band, but the overall sensitivity was higher for the 586-796nm wavelength band at each melanosome volume fraction. Sensitivity to changes in melanin was lower in overall magnitude for the 454-500nm wavelength band than for the 586-796nm wavelength band regardless of the dermal oxygenation parameter.

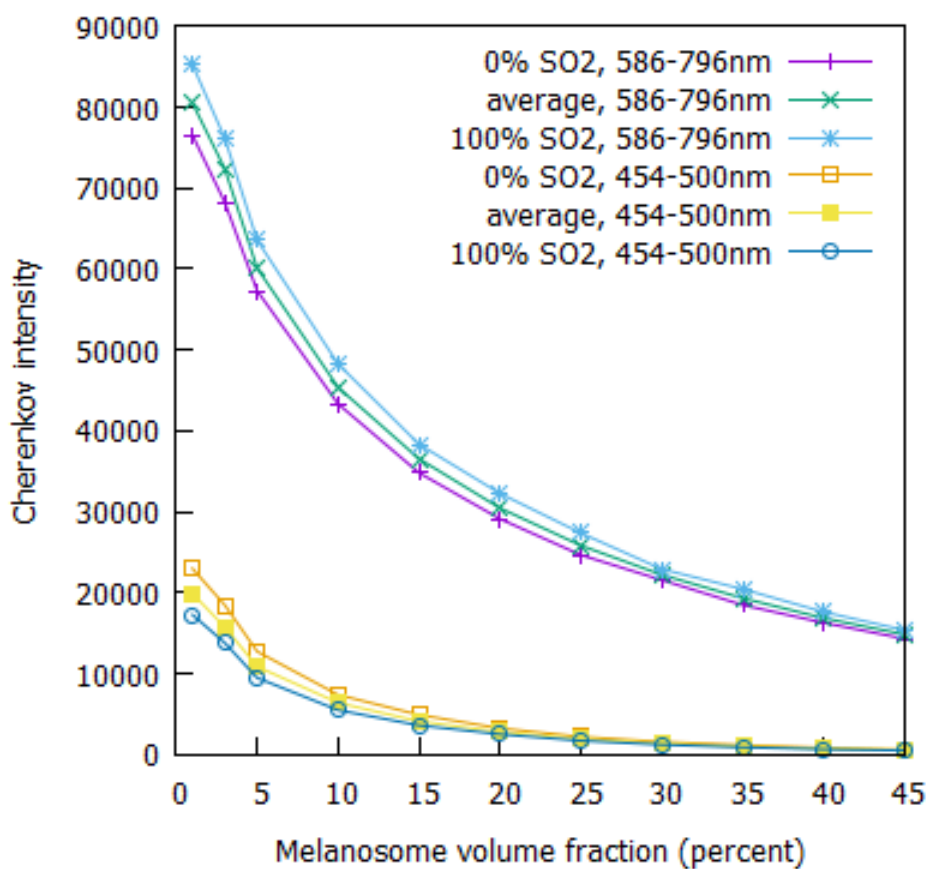


Figure 4-10. Emitted Cherenkov intensity per incident particle as a function of melanosome volume fraction. Curves are plotted for fully deoxygenated hemoglobin (0% SO₂), fully oxygenated hemoglobin (100% SO₂), and the average over all SO₂ values. The intensity curves are shown separately for Cherenkov radiation generated in the 454-500nm range and the 586-796nm range.

IV. Discussion

The spectral distribution of Cherenkov light emitted from skin tissue resembles the spectrum of diffusely reflected light from skin more closely than it does the familiar Cherenkov spectrum seen from water (figure 6). Cherenkov emission is more sensitive to hemoglobin than diffuse reflection because diffusely reflected light includes a large amount of backscattered light from the epidermal layer, while Cherenkov light only passes through the epidermal layer when leaving the skin surface. As a spectroscopic probe of tissue oxygenation, Cherenkov radiation may be able to provide effective insights into biological response to radiation therapy.

The sensitivity of Cherenkov radiation to changes in melanin is higher than the oxygen saturation sensitivity in the two broad wavebands analyzed, but radiation therapy does not significantly change the melanin-based absorption of skin during the treatment course¹⁷. Late response to treatment does cause statistically significant changes to occur after one year post-treatment, associated with depigmentation, but during the treatment course, only the absorption by hemoglobin increases significantly.¹⁷ Erythema reactions may be more likely to occur following an approximately 20 percentage increase in the oxygen saturation,¹⁸⁻²⁰ so predicting skin reactions early in the treatment may be possible through Cherenkov imaging.

The response to treatment of skin surface lesions, such as keloids and skin cancers, could be monitored using the change in oxygen saturation measured

using Cherenkov emissions. Keloids have approximately half the oxygen saturation of adjacent normal skin, and keloids that successfully respond to treatment will return to typical oxygen saturation values²¹. While melanoma, which has approximately 15 percentage lower oxygen saturation compared to adjacent normal tissue,²² is not usually treated with radiation, basal cell and squamous cell carcinoma can have approximately 5 percentage lower than typical oxygen saturation²³.

The ability to detect a 5% to 20% SO₂ change in oxygen saturation depends on the contrast between the surface lesion and the surrounding normal tissue in the Cherenkov images. We simulated images for a circular 3cm diameter keloid, defined by a 20% oxygen saturation lesion surrounded by normal tissue with 40% oxygen saturation (figure 11). The figure shows the expected contrast for differing levels of melanin in the skin, after adjusting the exposure time to rescale the normal tissue to equal intensities across the image series. Contrast decreases with increasing melanin. Contrast, defined here as the ratio of the difference in lesion and background intensity to the background intensity, is 2.18%, 1.93%, and 1.80% in the 586-796nm waveband and 5.78%, 5.69%, and 5.27% in the 454-500nm for light, medium, and dark skin, respectively. The lesion will emit less Cherenkov radiation than the normal tissue in the 586-796nm wavelength band, while the lesion is brighter than the normal tissue in the 454-500nm wavelength band.

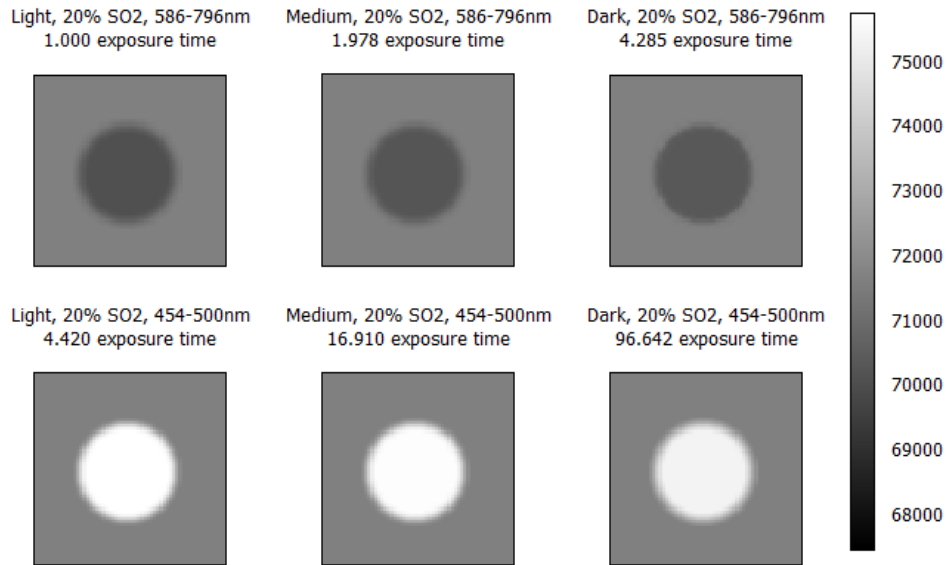


Figure 4-11. Cherenkov surface emission distributions in the 586-796nm waveband and the 454-500nm waveband, with 20% SO₂ in the central 3cm diameter circle of each image and 40% SO₂ baseline in the surrounding surface. The images are normalized to equal intensity in the 40% SO₂ surrounding surface, and the normalization factor shows the increasing relative imaging exposure time to compensate for absorption by increased melanin content and the sensitivity of each waveband. Variations are shown for light, medium, and dark skin containing, respectively, 2.5%, 15%, and 30% melanosome volume fraction of the epidermis. The grayscale units are total emitted Cherenkov photons per mm² for an incident 6MV beamlet of fluence 10⁶ x-rays per mm², multiplied by the relative exposure time shown above each image.

We simulated lesion oxygen saturation typical of a basal or squamous cell carcinoma for the same image series by setting the lesion to 35% SO₂ compared to normal tissue 40% oxygen saturation (figure 12). In this case of

5% SO₂ deficit, the contrast between the normal tissue background and the lesion is less than 1.5%. At 586-796nm wavelengths the contrast is only 0.54%, 0.49%, and 0.46% for light, medium, and dark skin, respectively, while the 454-500nm wavelength band has contrast of 1.44%, 1.41%, and 1.31% for the respective skin types. These simulated images use ideal detection conditions, which ignores the effects of noise that degrades the visibility of low contrast objects.

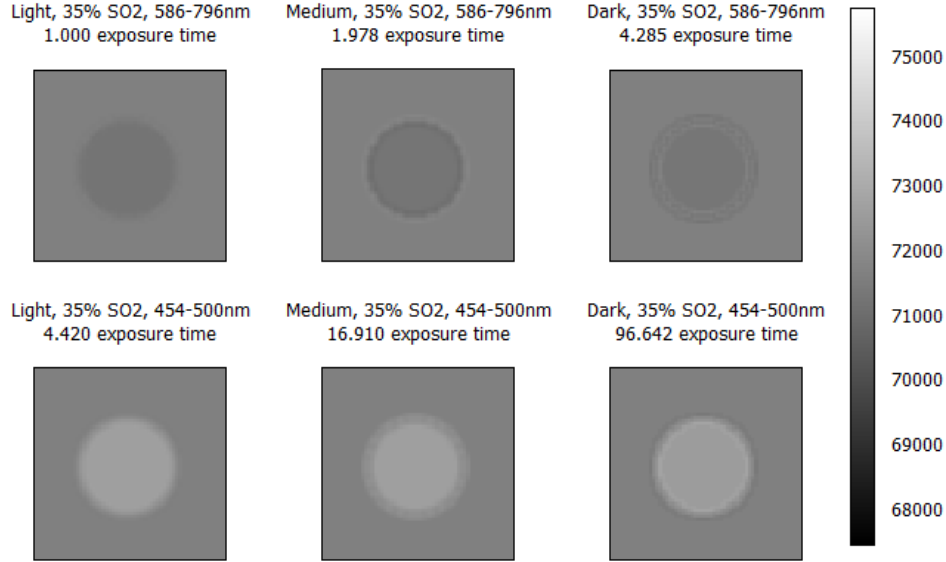


Figure 4-12. Cherenkov surface emission distribution contrast for a central circular region of 35% SO₂ and 40% SO₂ surrounding baseline. Variations are shown for waveband (586-796nm and 454-500nm) and melanosome volume fraction (light, medium, and dark skin). Scaling matches the images in figure 11.

To estimate the relative signal strength we evaluate the noise associated with Poisson photon statistics, which has a statistical variance equal to the mean number of photons. As a signal-strength metric, we calculate the estimated signal-to-noise ratio (SNR) for each case based on the Rose model²⁴,

$$SNR = C\sqrt{A\langle n_b \rangle} \quad 16$$

which depends upon the lesion contrast C , the lesion area A , and the average background photon density n_b . The calculated SNR (Table I) varies with the

oxygen-deficit in each lesion type, for each waveband, and across the melanin-content of the skin. Notably the 454-500nm waveband signal strength for lightly pigmented skin is 13% higher than the 586-796nm waveband, while with medium pigmented skin the 586-796nm waveband has 13% higher signal than the 454-500nm waveband. For the case of darkly pigmented skin the signal strength is 32% higher for the 586-796nm waveband than for the 454-500nm waveband. The optimal waveband to focus on for Cherenkov imaging in oxygen-deficit lesions depends on the melanin content of the skin.

Table 4-I. Signal-to-noise ratio of Cherenkov radiation emission in de-oxygenated skin lesions. Variation with melanin is parameterized into light, medium, and dark skin. Two principle wavebands, 586-796nm and 454-500nm, are compared for each skin type.

		Light	Medium	Dark
20% SO ₂ lesion	586-796nm	106.6	68.0	44.0
	454-500nm	120.3	60.5	33.2
35% SO ₂ lesion	586-796nm	26.7	17.0	11.0
	454-500nm	30.1	15.1	8.30

Another consideration for Cherenkov imaging is the imaging angle. The directional distribution of Cherenkov light emitted from skin indicates the directional sensitivity for imaging Cherenkov radiation. Our simulations showed that Cherenkov light is emitted in the forward direction more than diffusely reflected light. For emission making an angle of 35 degrees or close to the surface, Cherenkov emission becomes less intense than the intensity

from an ideal diffuse scattering material. Ideal diffuse scattering results in equal radiance emitted in all directions ($\text{cm}^{-2}\text{Sr}^{-1}$), considering that the apparent size of the surface changes inversely with the cosine of the angle from the surface normal, but our results indicate that Cherenkov apparent intensity will continually increase with increasing angles from the skin surface and approach a maximum at the surface normal. The slight impact on apparent Cherenkov intensity from variations in the imaging angle may contribute to poor resolution of low-contrast surface lesions at large imaging angles from the surface normal.

The lesion visibility in an image depends on the blur at the edges of the lesion. The Cherenkov emission area extends over a larger area of skin than the incident x-ray beam, which indicates some amount of blurring will appear in the images. Measurement of the Cherenkov radiation's profiles shows a FWHM of 1.8 mm compared to the 1.0 mm FWHM of the skin surface isodose curves, or a loss of spatial resolution of approximately 0.4 mm from the radiation field edge. However, the impact of spatial resolution depends on both the lesion size and contrast. Surface lesions undergoing radiotherapy will typically be large enough that the loss of 0.4mm spatial resolution would negligibly affect lesion visualization.

V. Conclusions

Cherenkov radiation generated in skin by an external beam of radiation provides a means of quantitatively measuring biological properties. Melanin

absorption in skin occurs in the epidermis, and the absorption coefficient is inversely proportional to the cube of wavelength. For this reason, diffuse reflectance spectral measurements using an external illumination source are limited to long wavelengths where melanin weakly absorbs because the incident light must cross the epidermis on the way into the body and again on the way out of the body. However, Cherenkov radiation generated throughout the irradiated tissues can carry the signal from the dermal tissues to the surface, passing through the melanin layer only once, which mitigates the loss at short wavelengths. Cherenkov radiation may provide a way to interrogate physiological parameters in the skin, particularly at short wavelengths.

We investigated the emitted Cherenkov intensity from the skin surface in terms of the surface emission angle, the apparent position on the skin surface, and the wavelength distributions resulting from variations in the hemoglobin oxygen saturation and the melanin content of the skin. The spectral distribution of Cherenkov radiation emitted from tissue can support two distinct wavebands that allow oxygen saturation estimates and the possibility of tracking treatment progress of skin lesions. We also incorporated estimates for the loss of Cherenkov sensitivity with increased melanin content for each waveband. The estimated lesion contrast variation with oxygen saturation, parameterized by wavelength band and the amount of epidermal melanin, has a potential application in lesion response detection

during radiotherapy. For oxygen-deficit skin lesions in lightly pigmented skin, the 454-500nm waveband produces a stronger signal than the 586-796nm waveband. In moderately to darkly pigmented skin the 586-796nm waveband produces the stronger signal.

VI. Acknowledgments

We would like to thank the Nuclear Science and Engineering Institute at the University of Missouri for providing funding for this research through a GAANN grant from the US Department of Education.

VII. References

- ¹ L.A. Jarvis, R. Zhang, D.J. Gladstone, S. Jiang, W. Hitchcock, O.D. Friedman, A.K. Glaser, M. Jermyn, B.W. Pogue, "Cherenkov video imaging allows for the first visualization of radiation therapy in real time," *International journal of radiation oncology, biology, physics* **89**, 615-622 (2014).
- ² A.K. Glaser, R. Zhang, D.J. Gladstone, B.W. Pogue, "Optical dosimetry of radiotherapy beams using Cherenkov radiation: the relationship between light emission and dose," *Physics in medicine and biology* **59**, 3789-3811 (2014).
- ³ F.H. Attix, W.C. Roesch, E. Tochilin, *Radiation dosimetry*, 2d ed. (Academic Press, New York, 1966).
- ⁴ M.J. Berger, Hubbell, J.H., Seltzer, S.M., Chang, J., Coursey, J.S., Sukumar, R., Zucker, D.S., and Olsen, K., *XCOM: Photon Cross Section Database*. (National Institute of Standards and Technology, Gaithersburg, MD, 2010).
- ⁵ M.J. Berger, Coursey, J.S., Zucker, M.A., and Chang, J, *ESTAR, PSTAR, and ASTAR: Computer Programs for Calculating Stopping-Power and Range Tables for Electrons, Protons, and Helium Ions*. (National Institute of Standards and Technology, Gaithersburg, MD, 2005).

- 6 K. Nakamura, "Review of Particle Physics," *Journal of Physics G: Nuclear and Particle Physics* **37**, 075021 (2010).
- 7 A.N. Bashkatov, E.A. Genina, V.V. Tuchin, "OPTICAL PROPERTIES OF SKIN, SUBCUTANEOUS, AND MUSCLE TISSUES: A REVIEW," *Journal of Innovative Optical Health Sciences* **04**, 9-38 (2011).
- 8 J. Motz, H. Olsen, H. Koch, "Electron Scattering without Atomic or Nuclear Excitation," *Reviews of Modern Physics* **36**, 881-928 (1964).
- 9 S.A. Prahl, M. Keijzer, S.L. Jacques, A.J. Welch, "A Monte Carlo Model of Light Propagation in Tissue," 1989).
- 10 S.V. Patwardhan, A.P. Dhawan, P.A. Relue, "Monte Carlo simulation of light-tissue interaction: three-dimensional simulation for transillumination-based imaging of skin lesions," *IEEE transactions on biomedical engineering* **52**, 1227-1236 (2005).
- 11 E. Salomatina, B. Jiang, J. Novak, A.N. Yaroslavsky, "Optical properties of normal and cancerous human skin in the visible and near-infrared spectral range," *J Biomed Opt* **11**, 064026 (2006).
- 12 S.L. Jacques, "Corrigendum: Optical properties of biological tissues: a review," *Physics in medicine and biology* **58**, 5007-5008 (2013).
- 13 E. Hecht, *Optics*, 4th ed. (Addison-Wesley, Reading, Mass., 2002).
- 14 R.M. Pope, E.S. Fry, "Absorption spectrum (380–700 nm) of pure water. II. Integrating cavity measurements," *Applied optics* **36**, 8710-8723 (1997).
- 15 M. Born, E. Wolf, *Principles of optics; electromagnetic theory of propagation, interference, and diffraction of light*, 2d rev. ed.
- 16 A. Morel, "Optical properties of pure water and pure sea water," *Optical aspects of oceanography* **1**, 1-24 (1974).
- 17 M. Kawashima, M. Nozaki, K. Komazaki, R. Yamamuro, K. Ishizuna, M. Kojima, "Quantitative Assessment of Chronic Skin Reactions Including Erythema and Pigmentation after Breast Conserving Therapy," *Advances in Breast Cancer Research* **05**, 121-128 (2016).

- 18 M.S. Chin, B.B. Freniere, Y.C. Lo, J.H. Saleeby, S.P. Baker, H.M. Strom, R.A. Ignatz, J.F. Lalikos, T.J. Fitzgerald, "Hyperspectral imaging for early detection of oxygenation and perfusion changes in irradiated skin," *J Biomed Opt* **17**, 026010 (2012).
- 19 D. Yohan, A. Kim, E. Korpela, S. Liu, C. Niu, B.C. Wilson, L.C. Chin, "Quantitative monitoring of radiation induced skin toxicities in nude mice using optical biomarkers measured from diffuse optical reflectance spectroscopy," *Biomed Opt Express* **5**, 1309-1320 (2014).
- 20 L.C.L. Chin, E.K. Cook, D. Yohan, A. Kim, C. Niu, B.C. Wilson, S.K. Liu, "Early biomarker for radiation-induced wounds: day one post-irradiation assessment using hemoglobin concentration measured from diffuse optical reflectance spectroscopy," *Biomedical Optics Express* **8**, 1682 (2017).
- 21 C.K. Hsu, S.Y. Tzeng, C.C. Yang, J.Y. Lee, L.L. Huang, W.R. Chen, M. Hughes, Y.W. Chen, Y.K. Liao, S.H. Tseng, "Non-invasive evaluation of therapeutic response in keloid scar using diffuse reflectance spectroscopy," *Biomed Opt Express* **6**, 390-404 (2015).
- 22 A. Garcia-Uribe, E.B. Smith, J. Zou, M. Duvic, V. Prieto, L.V. Wang, "In-vivo characterization of optical properties of pigmented skin lesions including melanoma using oblique incidence diffuse reflectance spectrometry," *J Biomed Opt* **16**, 020501 (2011).
- 23 A. Garcia-Uribe, N. Kehtarnavaz, G. Marquez, V. Prieto, M. Duvic, L.V. Wang, "Skin cancer detection by spectroscopic oblique-incidence reflectometry: classification and physiological origins," *Appl Opt* **43**, 2643-2650 (2004).
- 24 A.E. Burgess, "The Rose model, revisited," *J Opt Soc Am A Opt Image Sci Vis* **16**, 633-646 (1999).

CHAPTER 5: External electron beam induced Cherenkov emission from the two-layer cutaneous tissue model

The previous chapter considered Cherenkov emission from skin undergoing irradiation with an external beam of 6MV x-rays generated from a medical linear accelerator, but often superficial treatments use an external beam of electrons. This chapter focuses on the same two-layer cutaneous model as the previous chapter, but the impinging 6MV x-ray beamlet is replaced with an impinging 6MeV electron beamlet.

I. Cherenkov emission for electron beams and sensitivity to tissue parameters

We simulated a $1 \times 1 \text{ mm}^2$ electron beamlet, which contained 10^4 electrons with an initial energy of 6MeV, normally incident to the cutaneous layers. Each simulated electron traveled its full range in tissue and was terminated either after depleting its energy or once it backscattered into air.

I.A. Cherenkov generation at depth

The spatial distribution of Cherenkov intensity throughout the material varies with depth into the medium from the air-surface and with lateral distance from the center of the electron beamlet (figure 1, left). Compared to the distribution from x-ray beams (figure 1, right), the electron beams generate Cherenkov radiation nearest the surface with decreasing intensity

at depth, while x-ray beams have a build-up region throughout the depth of the skin.

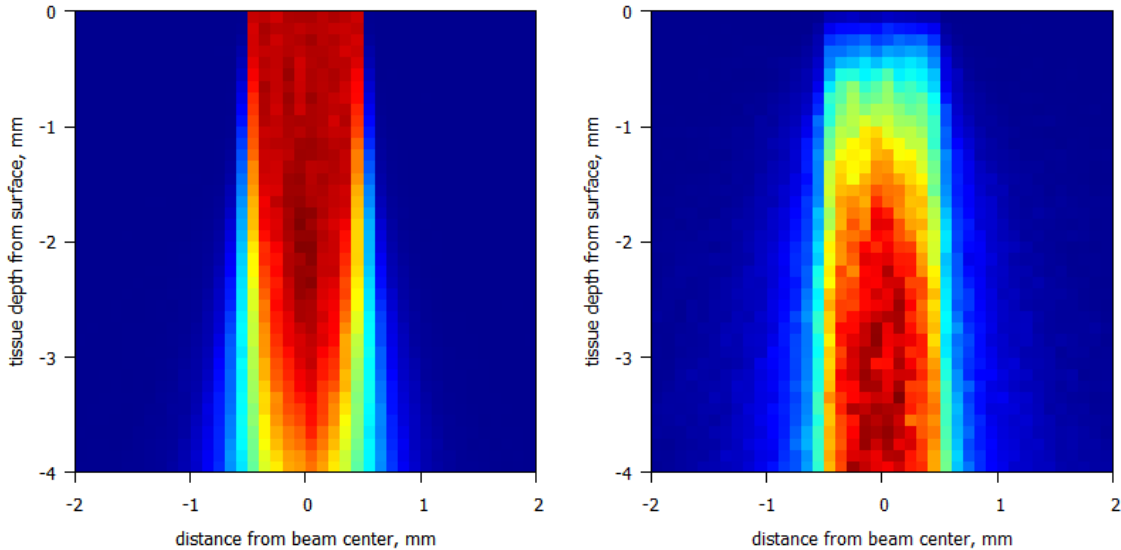


Figure 5-1. Cherenkov intensity distributions at the moment of generation in tissue for 6MeV electron beamlets (left) and 6MV x-ray beamlets (right). The top of each figure is the air-tissue interface (depth = 0) with depth on the vertical axis and the horizontal axis shows the lateral distance from the center of the 1mm wide beamlet.

I.B. Surface distributions

The surface distributions of the emitted Cherenkov photons are shown in figure 2 for the 6MV electron beam (figure 2, left) compared to the 6MeV x-ray beam (figure 2, right). The difference between these two distributions is the gradient in the intensity distribution, with the electron beam having a sharper gradient than the x-ray beam. The full-width at half-maximum (FWHM) of the electron-beam-generated Cherenkov emission is 1.3mm. For

the x-ray-generated Cherenkov emission, the FWHM is 1.8mm. Considering the depth distribution of Cherenkov generation described earlier (figure 1), the difference in emitted Cherenkov surface distributions (figure 2) can be attributed to the proximity to the surface of the Cherenkov photons when generated, since lateral travel of scattering photons increases with the distance traveled to reach the surface.

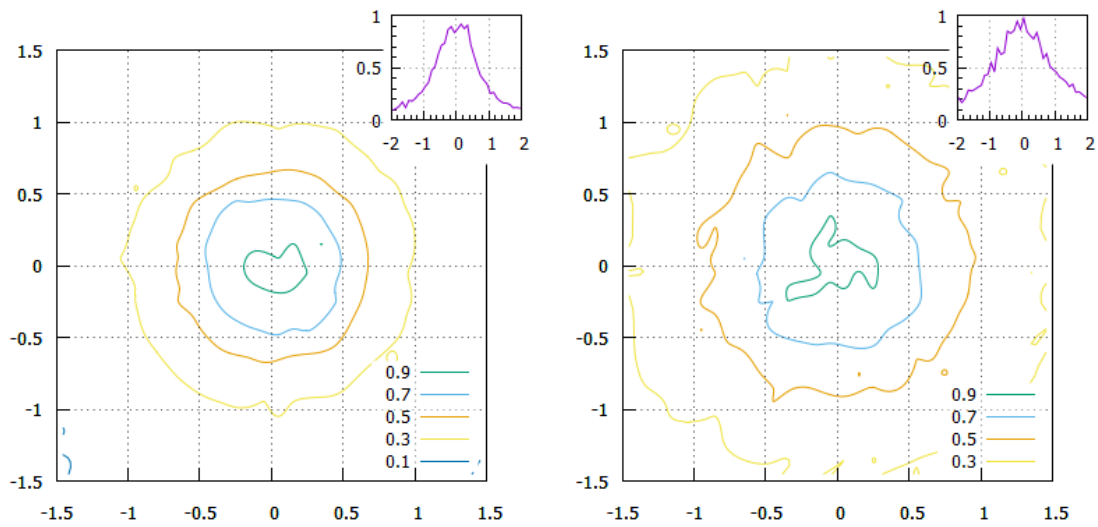


Figure 5-2. Top-down views of the air-tissue surface centered at the $1 \times 1 \text{ mm}^2$ beamlet, with insets showing the profile through the center of each corresponding plot. (left) Surface intensity contours of the emitted Cherenkov light generated by the 6MeV electron beam. (right) Cherenkov emission intensity from the surface for the 6MV x-ray beam. Both plots are normalized to the respective maximum emitted Cherenkov intensity.

I.C. Angular distributions

The angular distributions of emitted Cherenkov photons from skin (figure 3) essentially follow the expected distribution for diffuse reflection from skin. Compared to a Lambertian surface having ideal diffuse scattering, the photons scattering from skin are more forward scattered; the photon intensity per steradian for skin is greater than for a Lambertian surface at angles within 50 degrees of the surface normal. After normalizing the number of photons emitted to unity, Cherenkov emission with a 6MeV electron beam peaks at 0.35 Sr^{-1} and with a 6MV x-ray beam at 0.36 Sr^{-1} , compared to 0.34 Sr^{-1} for diffusely scattered light from skin or a Lambertian surface at 0.32 Sr^{-1} .

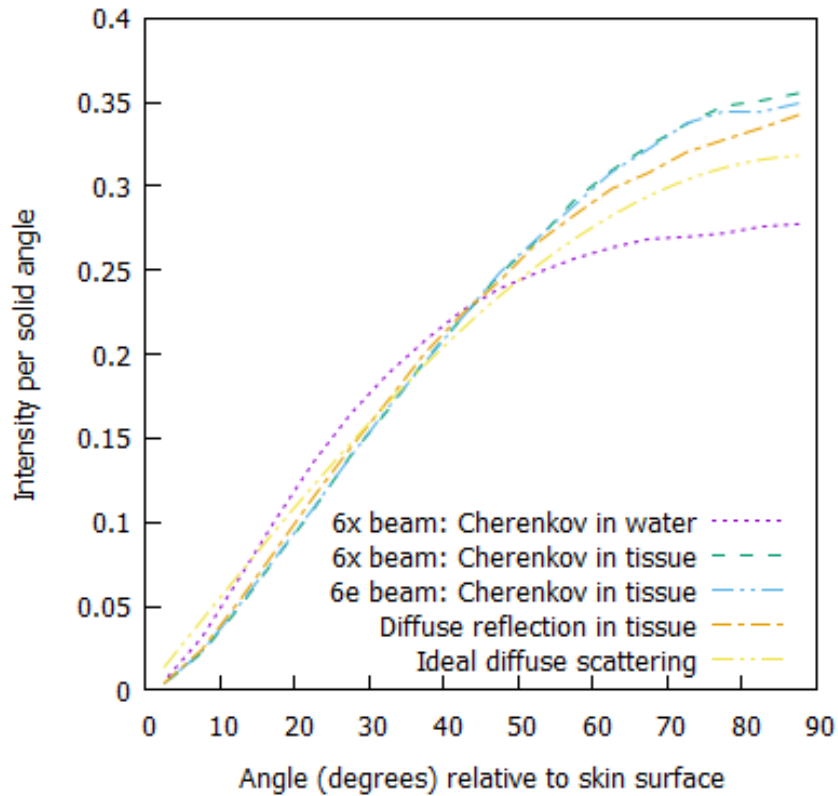


Figure 5-3. Emitted intensity plot of the directional distribution per unit solid angle (Sr^{-1}) of emitted light with 5 degree binning. The surface normal is designated as 90 degrees. The number of photons emitted are normalized to unity before calculating the emission per solid angle. Electron-beam-generated Cherenkov emission (6e beam) is shown in comparison to the x-ray-generated Cherenkov emission (6x beam).

I.D. Spectral distributions

The spectral distribution of Cherenkov photons emitted from the skin surface (figure 4) for electron-beam-generated Cherenkov photons closely matches the features found in x-ray beam generated Cherenkov photons,

after normalizing the simulated number of photons to unit photon emission, but there is slightly more Cherenkov attenuation at short wavelengths for Cherenkov radiation generated by x-ray beams. The reason may be that there is simply less attenuation of Cherenkov radiation electron beams where a much larger fraction of Cherenkov photons are generated closer to the surface than for x-ray beams.

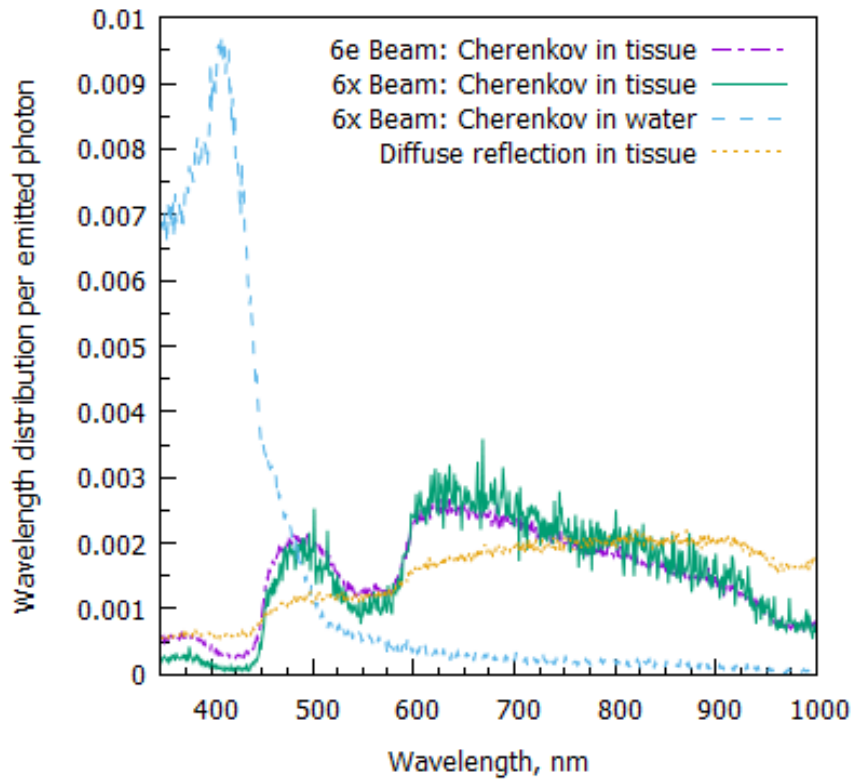


Figure 5-4. The photon spectral distribution of emitted light, ranging in wavelength from 350nm to 1000nm, for Cherenkov emission from tissue after generation by a 6MeV electron beam and a 6MV x-ray beam, Cherenkov emission from water after generation by the 6MV x-ray beam, and the diffusely reflected light from scatter in tissue. The plots are normalized to unit emitted photon.

II. Sensitivity of Cherenkov emission to surface lesion tissue parameters for electron beams

Using a convolution-superposition beam algorithm based on the 1x1 mm² electron beamlet and the surface distribution of Cherenkov radiation emission, we produced images for a 3 cm diameter skin lesion (figure 8). The circular center lesion is defined by 20% oxygen saturation in the dermal layer, and the surrounding normal tissue plane was defined as 40% oxygen saturation. Three representative skin pigmentations were selected: light (2.5% epidermal melanosomes by volume), medium (15%), and dark (40%). For the 586-796nm wavelength band, the expected contrast between the lesion and the surrounding tissue was found to be 1.83% in light skin, 1.44% in medium skin, and 1.19% in dark skin. In the 454-500nm wavelength band, the expected contrast was higher at 4.40% in light skin, 4.13% in medium skin, and 3.81% in dark skin.

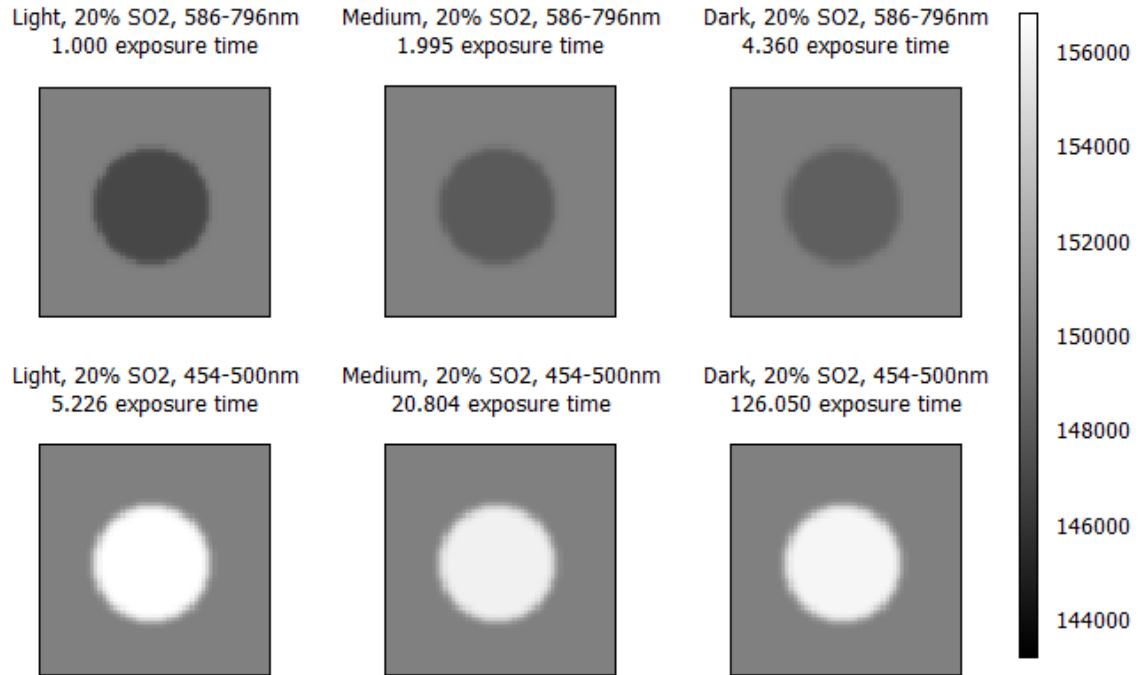


Figure 5-5. Cherenkov surface emission distributions in the 586-796nm waveband (top row) and the 454-500nm waveband (bottom row), with 20% SO₂ in the 3cm diameter keloid lesion and 40% SO₂ baseline in the surrounding normal tissue, which the grayscale values are centered around. Variations are shown for light (2.5% melanosome volume fraction), medium (15%), and dark (40%) skin.

We are able to determine the best wavelength band for signal strength from different skin pigmentations. For estimating the relative signal strength, accounting for the effects of noise associated with Poisson photon statistics in addition to the image contrast, we used the signal-to-noise ratio (SNR) based on the Rose model to calculate the SNR for each of the six representative images of the 20% SO₂ skin lesion (Table I). For light skin the

SNR was 6% higher in the 454-500nm wavelength band. In medium and dark skin, the 586-796nm wavelength band had a higher signal strength by 13% and 68%, respectively. Similar results were obtained for x-ray beams in Chapter 4, where the relative signal strength was 13% higher in the 454-500nm wavelength band for light skin, and the signal strength was 13% and 32% higher in the 586-796nm wavelength band for medium and dark skin, respectively.

Table 5-I. Signal-to-noise ratio of Cherenkov radiation emission in de-oxygenated skin lesions for an incident electron beam containing 10^4 electrons. Variations with melanin are parameterized into light, medium, and dark skin for different epidermal melanosome volume percentages and for the 586-796nm and 454-500nm wavebands.

		Light, 2.5%	Medium, 15%	Dark, 40%
20% SO ₂ lesion				
	586-796nm	187.8	105.1	58.6
	454-500nm	198.4	93.2	34.9
35% SO ₂ lesion				
	586-796nm	47.0	26.3	14.6
	454-500nm	49.6	23.3	8.73

III. Conclusions

Electron beams generate Cherenkov radiation that upon emission from the skin surface has similar angular, spatial, and spectral distributions to the Cherenkov radiation emitted from skin under irradiation by x-ray beams. The depth distribution of generated Cherenkov radiation follows the principles of the depth dose distribution for the x-ray beam and electron beam modalities; and most of the difference between the Cherenkov radiation

emitted by the two modalities is a consequence of the Cherenkov generation depth distribution. The angular distributions of Cherenkov radiation emitted by the two irradiation modalities are nearly identical, although x-ray generated Cherenkov radiation is slightly more intense in the direction of the surface normal. The surface distribution of Cherenkov radiation generated by electron beams has a sharper gradient than x-ray beam generated Cherenkov radiation. Cherenkov radiation emitted from the skin irradiated by electron beams has greater intensity at short wavelengths than Cherenkov emission that was induced by x-ray beams. These results are all consequences of shallow initial depths, which reduces absorption and scatter, of Cherenkov radiation produced by electron beams.

Within the specific wavelength bands that are sensitive to hemoglobin oxygen saturation, Cherenkov radiation that was generated by irradiation with x-ray beams shows less sensitivity to the effects of melanin, and electron beams produce lower relative signal strength in the 454-500nm wavelength band than x-ray beams produce. This does not have a large enough effect to contradict the finding that the short wavelength waveband of 454-500nm does produce a higher signal for lightly pigmented skin than the 586-796nm wavelength band, which holds for the electron beam irradiation modality as well as the x-ray beam irradiation modality discussed in Chapter 4.

CHAPTER 6: General Conclusions

I. General Discussion

Cherenkov radiation has been used in various applications since its discovery. Two applications relating to medical radiation dosimetry have been examined in this dissertation. In the case of Cherenkov radiation generated in organic plastic scintillation fibers, the Cherenkov radiation is contaminating noise in the scintillation signal, while in the case of Cherenkov emissions from an irradiated skin surface, the Cherenkov radiation provides measurable information that relates to the radiation entering the body through that surface and the molecular constituents of the irradiated skin. Monte Carlo simulations of the Cherenkov radiation in these media, with customized code written in the C programming language, have provided insights about the Cherenkov distributions that arise in these two practical applications.

Based on the results from simulations using a variety of parameters, we optimize the design of the real-time scintillating fiber dosimeter. Recommendations based on the parameters that minimize the Cherenkov radiation include the following:

- The fiber should be shifted to longer wavelengths beyond the peak region of the Cherenkov spectrum, as in the BCF-60 fiber.

- A high sensitivity photodiode detector improves with additional band filtering to eliminate signals outside the emission spectrum of the BCF-60 fiber.
- Organic scintillating fibers with a square cross-section have a much lower fractional Cherenkov component than round cross-sectional fiber, and the transmission losses are lower when the fiber width is varied, making them more robust over a range of sizes.
- Fibers with an edge length of less than 1 mm begin to have increased transmission losses, and while transmission losses decrease moderately for thicker fibers, there is a trade off with decreasing spatial resolution of the radiation field.

A two-layer tissue model examined the spectral distribution, angular distribution, and cutaneous propagation of Cherenkov radiation emitted from the skin induced by external radiotherapy beams. The primary purpose of the model was to explore the predominant factors in these properties of the emitted Cherenkov radiation. The results show the following:

- The wavelength distribution depends most strongly on the optical absorbers present in the dermal tissue, which are the oxy-hemoglobin and deoxy-hemoglobin found in blood perfusion in those tissues. The fraction of hemoglobin in the oxygenated state – the oxygen saturation of the perfused dermis – directly controls the intensity of Cherenkov radiation emitted in specific wavebands,

particularly 454-500nm and 586-796nm. The oxygen saturation in abnormal dermal tissue conditions is known to deviate from normal by up to 5-percentage in skin carcinomas and up to 20-percentage in keloids; both are conditions treated with external beam radiotherapy, which is known to generate Cherenkov radiation.

- In lightly pigmented skin, for x-ray beams and electron beams respectively, the 454-500nm waveband has a 13% and 6% higher signal-to-noise (SNR) ratio than the 586-796nm waveband. Moderately pigmented skin has a 13% higher SNR for the 586-796nm waveband, and darkly pigmented skin has a 33% and 68% higher SNR for the 586-796nm waveband.
- The angular distribution of Cherenkov radiation is only slightly more forward peaked than diffusely remitted light from tissue. Diffuse reflection and emitted light from tissue are slightly forward peaked relative to an ideal diffuse reflecting surface. Therefore, the angle used for Cherenkov imaging will not greatly affect light collection efficiency.
- The full-width at half-maximum of Cherenkov light generated by a 1.0mm x-ray beamlet is 1.8mm and for an electron beamlet is 1.3mm, while the full-width at half-maximum of both the surface dose and diffusely scattered light are 1.0mm. A blurring effect of up

to 0.4mm at the edges of the Cherenkov emission would be expected, which is insignificant relative to typical tumor sizes.

II. Recommendations for future research

The simulation results for the scintillating fiber dosimeter show variations of several fiber parameters, and experimental results with an undoped optical fiber validated the simulation results of the change in Cherenkov signal with incident beam angle. In the simulations at parameter values used in the detector prototype, we expect virtually no Cherenkov contamination, which indicates future work with the scintillating fiber detectors will not require corrections for Cherenkov contamination.

Our simulations using the two-layer tissue model of Cherenkov radiation emission explored the variation in Cherenkov emission for biological parameters. Cherenkov signal was sensitive to oxygen saturation of the dermis, with distinct wavebands producing stronger signals depending on the amount of melanin in the epidermis. Future work to validate the results would require the preparation of a tissue-like phantom that mimics the radiological properties as well as the optical absorption and scattering in cutaneous tissue.

VITA

Andy Wiles graduated with a Bachelor of Science in Physics and an Honors Minor in Interdisciplinary Studies from the University of Central Arkansas, Conway, AR, in May 2007. He completed a Master of Science in Nuclear Engineering in December 2012 and passed the American Board of Radiology Part-1 Exam for Medical Physics in 2012. He gave an oral presentation at the 2014 AAPM Annual Meeting titled “Monte Carlo Based Design of Efficient Scintillating Fiber Dosimeters,” at the 2015 AAPM Annual Meeting titled “A tissue model of Cherenkov emission from the skin surface during megavoltage x-ray radiotherapy,” at the 2017 AAPM Annual Meeting titled “Rapid High Resolution Quality Assurance Phantom and Protocol for 6D Robotic Couches,” and he presented a poster in 2017 at the 3rd Annual West Cancer Center Research Conference titled “Dosimetric Validation of Personalized 3D Printed High Dose Rate Brachytherapy Applicators.” He will receive a Doctorate of Philosophy in Nuclear Engineering at the University of Missouri-Columbia in December 2017. Starting in November of 2016, he began employment as a medical physicist with Methodist LeBonheur Healthcare & West Cancer Center in Memphis, TN.